8-1-2018

Developing a Femtosecond Stimulated Raman Spectroscopy Experiment for Solid State Materials

Daniel Hammerland
University of Denver

Developing a Femtosecond Stimulated Raman Spectroscopy Experiment for Solid State Materials

A Thesis

Presented to

the Faculty of Natural Sciences and Mathematics

University of Denver

In Partial Fulfillment

of the Requirements for the Degree

Master of Science

by

Daniel Hammerland

August 2018

Advisor: Mark Siemens

Author: Daniel Hammerland
Title: Developing a Femtosecond Stimulated Raman Spectroscopy Experiment for Solid State Materials
Advisor: Mark Siemens
Degree Date: August 2018

Abstract

Femtosecond Stimulated Raman Spectroscopy (FSRS) is a ultrafast spectroscopy technique first implemented by chemists to understand isomerization and other ultrafast molecular morphology changes by resolving vibrational dynamics[1, 2, 3]. FSRS has an unparalleled temporal and spectral resolution [4, 1, 5, 6] that arises as a result of a clever combination of picosecond and femtosecond pulses. However, despite this capability, FSRS has yet to be applied to modern materials in condensed matter physics. This thesis explores the design and implementation of FSRS to study two-dimensional materials in order to measure their quantum confined vibrational dynamics on utlrafast time scales.

Contents

List of Figures

Chapter 1

Overview

Innovation arises when the ideas from one field inspire another, as happened when semiconductor physicists adapted nuclear magnetic resonance spectroscopy from microwave to optical frequencies, leading to the development of multidimensional coherent spectroscopy [7, 8, 9].

This thesis centers around a similar attempt to adapt Femtosecond Stimulated Raman Spectroscopy (FSRS) to study of novel solid state materials. FSRS probes a materials structure with femtosecond temporal resolution by acquiring vibrational spectra of transient states. Because of this ability, FSRS has unveiled intermediate states in biological and chemical process, [10, 4, 1, 11, 12, 13, 3, 14, 15, 16].

Sensitive techniques find their idyllic match in interesting samples. In 2004, the isolation of the first atomically thin crystal, graphene [17], began a revolution in condensed matter physics, giving way to a tide of quantum confined materials like MoS_2 [18] and ReS_2 [19]. The broken symmetry in these materials and quantum confinement that both result from the atomically thin nature of these materials leads to many interesting phenomena, such as Dirac Fermions [20] and ballistic thermal transport [21, 22, 23].

Further, 2D materials have a remarkable promise for technological applications. The absence of chemical bonds between adjacent layers makes them ideal for creating heterostructures[24], electronic devices whose properties are finely tuned by stacking different layers of materials on top of each other and even by orienting the planes at different angles [25]. In bulk materials, bond dislocations between layers of different materials leads to device instability[26]. This problem is mitigated in 2D materials, making them ideal for next generation electronic devices [27, 28].

However, before these materials can be functionally integrated into technology, a strong understanding of their properties is needed. While extensive work has gone into theoretically modeling of nanoscale thermal transport [29, 30, 31], experimental results are lacking [23]. Time resolving phonon population dynamics on the characteristic timescales of the heat transfer in these materials would provide strong insight into quantum confined thermal transport[23].

Adapting FSRS to work on solid state materials would capture high resolution phonon spectra with femtosecond resolution, providing much needed experimental verification of models [29, 30, 31] while also helping us understand these highly interesting 2D materials. I have spent the last two years designing and building a FSRS apparatus for studying phonon dynamics in 2D materials, the results of which are presented in this thesis. Chapter 2 begins with an overview of nonlinear optics, where all the effects relevant to experimental implementation of FSRS will be derived. Chapter 3 discusses Raman Spectroscopy. This is followed by a derivation of Stimulated Raman Scattering. Chapter 4 will discuss 2D materials and outline the procedure followed for fabricating some of the lab's 2D material samples. This will include the characterization of the samples with Spontaneous Raman Spectroscopy. Chapters 5 reviews the theoretical basis for FSRS to set the stage for Chapter 6, where the designs and results from the solid state FSRS experiment are discussed

at length. Chapter 7 presents nonlinear processes' ability to bypass the Heisenberg Uncertainty Principle in an approachable manner and overviews the criteria for when a nonlinear signal can achieve sub Heisenberg resolution. The final chapter serves as an appendix and discusses methods and background for the experiment.

Chapter 2

Nonlinear Optics

The fundamental interaction of an electric field with a medium is described by the equation,

$$P = \epsilon_0 \chi E, \tag{2.1}$$

where ϵ_0 is the permeability of free space, χ is the electric susceptibility, and E is the applied electric field. While a powerful equation, it exists at an introductory level of understanding the interactions of electric fields and matter. A more insightful version of the equation can be constructed through the power series expansion of the polarization,

$$P = \epsilon_0(\chi_1 E + \chi_2 E^2 + \chi_3 E^3 + ...). \tag{2.2}$$

From this equation a wealth of interesting phenomena and rich physics have been gained where the linear interactions of Equation 2.1 are retained, while also gaining insight into a materials response to numerous fields, the nonlinear response. The magnitude of the nonlinear response, mathematically represented by the factor χ^n,

depends strongly on a materials energy structure and symmetry [32]. As a result, nonlinear responses have a remarkable ability to assess the energy structure of a material beyond what is capable with linear spectroscopies[7, 11, 33].

The high intensity fields required to induce these nonlinear interactions in a sample lead to the development of pulsed laser systems. In these lasers average powers can be moderately low as for the majority of the time there is no field emitted. Then, there is an abrupt surge where for a brief time power outputs can raise between megawatt and gigawatt levels[34]. The temporal confinement of these fields allows for nonlinear experiments to not just study material structure and symmetry in a steady state system, but to also reveal dynamics that happen on matters' fundamental time scales, ranging from hundreds of picoseconds to a a few femtoseconds[35], allowing for direct visualization of intermediate states in materials ranging from proteins [14] to short lived quasiparticles [8].

2.1 An intuitive approach to nonlinear optics

2.1.1 χ^n as a response of n-fields

An obvious feature of Equation 2.2 is the presence of n E fields for each corresponding χ^n term. While initial inspection of Equation 2 might leave one suspecting that E and all fields in E^n are be identical, this is not necessarily the case. A more general view would be thinking of each n^{th} order term as the mixing of n different fields in a material. As the mixing of these n fields in a material results in a field, arising in the form of a polarization, it is common to think of a n^{th} order process as $n+1$ wave mixing. This is commonly depicted through energy diagrams, as seen in Figure 2.1

Figure 2.1: Energy diagram depicting the parametric processes of a) sum frequency generation, b) second harmonic generation, and c) difference frequency generation

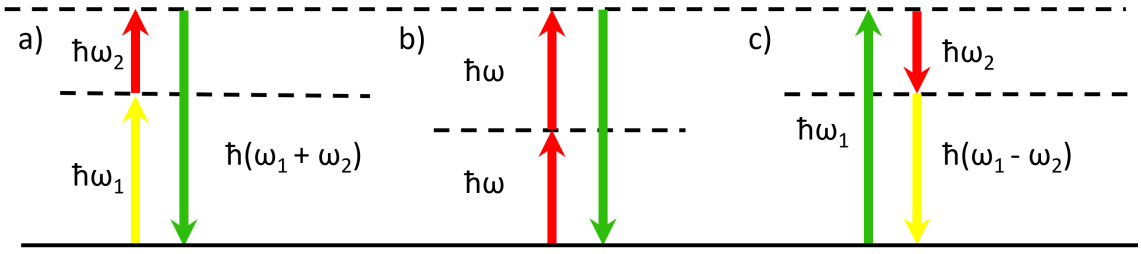

In a n^{th} order nonlinear process, an electron, presumed to be starting in the ground state, must interact with n distinct fields before it can relax back down to the final state. The final state will be the initial state for a parametric process or a different state for a non-parametric process. In this thesis, only parametric processes will be discussed. Mathematically, each χ^n in Equation 2 is a rank n tensor. A simple understanding of the processes associated with each term in Equation 2 can arise from considering each χ^n as the relation between the induced polarization of a material relative to the n fields inducing it [35].

The magnitude of the nonlinear susceptibility, χ^n, can be directly tied to the chance of these n interactions occurring without the electron relaxing to its ground state first[32]. Generally, the more fields being mixed, the lower the chance of that process occurring. Thus, higher order processes require higher intensity fields. The energy structure of a system also greatly affects the efficiency of a nonlinear interaction. Electrons can be excited to either electronic or vibrational states, which have relatively long lifetimes. Alternatively, the electrons can be excited to virtual states that are exceptionally short lived. This is why nonlinear optics has such a remarkable ability to probe the underlying energy structure of a system with such immaculate detail.

2.1.2 Nonlinearities as quantum path selection

In any n^{th} order nonlinear interaction, n fields mix to produce a certain polarization. These photons can be from the same beam, or from numerous beams mixing. In either case, however, there usually exist numerous quantum pathways for which the electron can be driven. Depending on the pathway that is selected, the emitted polarization can vary drastically in its emitted direction, frequency, and intensity.

Keeping track of these pathways can be challenging, especially for higher order nonlinearities where the number of pathways can increase rapidly. Feynmann diagrams are a particularly useful method for quantum pathway bookkeeping [35]. These diagrams are distinct from those seen in particle physics, but the general idea is similar. Time travels in the vertical direction and a state is represented by a pair of numbers. Both numbers being the same represents a population and a set of mixed numbers corresponds to a population. The number on the left will be the ket of a state and the number on the right will be the bra of a state.

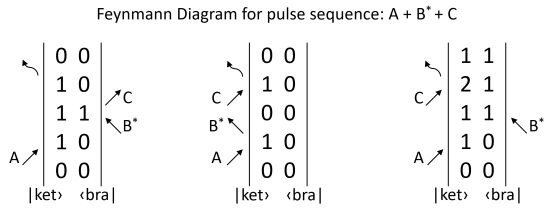

Figure 2.2: Feynmann diagrams depicting the various quantum pathways for $A+B^*+C+D^*=0$. Image adapted from Ref. [36]

Nonconjugate pulses will raise a ket to a higher level and will lower a bra, whereas conjugated pulses will lower a bra and raise a ket. Arrows pointing out of the diagram represent energy leaving the system and arrows directed in represent energy entering the system. For an n^{th} order process there will be n arrows with the final arrow representing the induced polarization emitted by the system that will be detected. It is important

to note that a specific pulse sequence can support numerous quantum pathways, as shown in Figure 2.2. This describes the nonlinear pathway $A + B^* + C = D_{signal}$, a commonly observed pathway in coherent nonlinear spectroscopy [36].

2.2 Nonlinear response for second and third order processes

Before diving too deep into the mathematical framework of nonlinear optics, it should be noted that no citations will be provided for derivations throughout this thesis. References [34, 32, 35] were used as guides and can be examined for further details. The nonlinear response of a medium to an applied electromagnetic wave is described by,

$$\nabla^2 E - \frac{\epsilon}{\epsilon_0 c^2}\frac{\partial^2 E}{\partial t^2} = \frac{1}{\epsilon_0 c^2}\frac{\partial^2 P_{NL}}{\partial t^2}, \tag{2.3}$$

where E is the complex applied electric field, ϵ is the susceptibility, and P_{NL} is the nonlinear polarization of the material. Additionally, it is assumed that the field and medium are interacting non-resonantly, as to have an instantaneous response with the medium. As a result of the instantaneous response, the pulses must be spatially and temporally overlapped in the medium.

A general electric field, E_j can be written completely as,

$$E_j = A_j(z)e^{i(k_j z - \omega_j t)} + A_j^*(z)e^{-i(k_j z - \omega_j t)}, \tag{2.4}$$

where the complex conjugate term has been included in order to obtain a real field. It should be noted, that conjugation is linear process and as a result, only one term

in Equation 2.4 needs be solved. Further, once E_j is inserted into an equation, it will often be immediately reduced to $A_j(z)$ multiplied by some exponential. It should also be noticed that amplitude of E_j, $A_j(z)$, varies weakly as it propagates. In the absence of a nonlinear polarization, this will merely result in an unperturbed electromagnetic wave. However, in a nonlinear medium, this weakly varying amplitude gives rise to energy conversions between different fields. This is the fundamental effect of nonlinear optics.

To completely utilize Equation 2.3, a solution for the polarization must be assumed,

$$P_n = 4\epsilon_0 d_{eff} A_m(z) A_p(z) e^{i\left(k_m + k_p)z - \omega_n t\right)}, \tag{2.5}$$

where once again the intensities of two fields are functions of propagation length. The term d_{eff} represent the matrix element from the $\chi^{(n)}$ susceptibility tensor, which describe the magnitude of the nonlinear response and also handles polarization effects. This means that E_i's do not necessarily have to be of identical polarization. Each term here must be calculated for all polarizations and wavelengths inside the beams bandwidth in order to assess the total nonlinear interaction for an experimental design, although most calculations can be simplified to a single frequency field with already correctly assumed polarization relations. This is done here for simplicity, and it is chosen that two driving fields, E_m and E_p, gives rise to a polarization in the form E_n. This corresponds to a second order response as two fields are mixing to produce a third. The situation for higher order interactions will be discussed later on.

Inserting the first term of Equation 2.4 and all of 2.5 into the nonlinear wave Equation 2.3 yields,

$$\Big(\frac{\partial^2 A_n(z)}{\partial z^2} + 2ik_n\frac{\partial A_n(z)}{\partial z} - k_n^2 A_n(z) + \frac{\epsilon\omega_n^2}{c^2}A_n\Big)e^{i(k_n z-\omega_n t)} = \frac{-4\epsilon_0 d_{eff}\omega_n^2}{\epsilon c^2}A_m(z)A_p(z)e^{i\left(k_m+k_p)-\omega_n t\right)} \tag{2.6}$$

the terms $-k_n^2 A_n(z)$ and $\frac{\epsilon\omega_n^2}{c^2}A_n(z)$ cancel, as does the time dependence. It is now necessary to invoke the Slowly Varying Envelope approximation, in which the pulse duration is much larger than the wave packet carrier period. This approximation is reasonable for most laser pulses greater than a few femtoseconds with center wavelengths in the visible and near infrared, which is sufficient for all the pulses relating to this thesis. In this limit, the first term of Equation 2.6 becomes negligible. Solving for $\frac{\partial A_n(z)}{\partial z}$ yields,

$$\frac{\partial A_n(z)}{\partial z} = \frac{2i\epsilon_0 d_{eff}\omega_n^2}{\epsilon c^2}A_m(z)A_p(z)e^{i(k_m+k_p-k_n)z}. \tag{2.7}$$

This results is the coupled wave equation. The equation above applies to a second order response of a material where two photons, m and p, are parametrically added to emit a photon n. A similar result is found for the fields A_m and A_p,

$$\frac{\partial A_p(z)}{\partial z} = \frac{2i\epsilon_0 d_{eff}\omega_p^2}{\epsilon c^2}A_n(z)A_m^*(z)e^{-i(k_m+k_p-k_n)z} \tag{2.8}$$

and

$$\frac{\partial A_m(z)}{\partial z} = \frac{2i\epsilon_0 d_{eff}\omega_m^2}{\epsilon c^2}A_n(z)A_p^*(z)e^{-i(k_m+k_p-k_n)z}. \tag{2.9}$$

The final exponentials at the end of each of the above equations are of major importance; these are the phase matching conditions, which are a measure of the momentum mismatch between the different fields as they propagate. In the

ideal case, $k_m + k_p - k_n = 0$ there will be perfect phase matching and the energy transfer between the different fields will be optimized. In the realistic limit where $k_m + k_p - k_n \neq 0$ the energy transfer will oscillate as the beam propagates through a medium. The smaller the value of $k_m + k_p - k_n$, the further through the medium the beam can travel while experiencing gain, thus increasing the efficiency. For experimental design, this means that minimally the nonlinear medium must be rotated in order to optimize the response.

This is clearly a very specific result and by expanding this result to a more general scenario, a much stronger physical intuition of of the quantum mechanics at play here is gained. In the situation described by Equations 2.7-2.9, the parametric quantum pathway defined by $k_m + k_p = k_n$ is followed. From this form, a mathematical analogy can be followed to create the general coupled wave equation,

$$\frac{\partial A_n(z)}{\partial z} = \frac{2i\epsilon_0 d_{eff}\omega_i^2}{\epsilon c^2} \prod_{m=1}^{nc} A_m \prod_{p=1}^{c} A_p^*(z) e^{i(\sum_{m=1}^{nc} k_m - \sum_{p=1}^{c} k_p - k_n)z}, \tag{2.10}$$

where nc and c are the number of non-conjugate and conjugate terms in the specific quantum pathway of interest.

2.2.1 Second order processes

Several second order nonlinear processes are of particular importance to this thesis. Suppose fields of two frequencies, ω_1 and ω_2, such that there is a net electric field of

$$E_{tot} = E_1 e^{-i\omega_1 t} + E_2 e^{-i\omega_2 t} + E_1^* e^{i\omega_1 t} + E_2^* e^{i\omega_2 t}, \tag{2.11}$$

where the E's contain the transverse variation. Take a nonlinear polarization of the form

$$P = \epsilon_0 \chi^{(2)} E_{tot}^2. \tag{2.12}$$

By expanding out the E_{tot}^2 term, Equation 2.12 becomes,

$$P = \epsilon_0 \chi^{(2)} \Big[E_1^2 e^{-2i\omega_1 t} + E_2^2 e^{-2i\omega_2 t} + E_1 E_2 e^{-i(\omega_1+\omega_2)t} + E_1 E_2^* e^{-i(\omega_1-\omega_2)t} + E_1^{*2} e^{2i\omega_1 t} + E_2^{*2} e^{2i\omega_2 t} + E_1^* E_2^* e^{i(\omega_1+\omega_2)t} + E_1^* E_2 e^{i(\omega_1-\omega_2)t} \Big]. \tag{2.13}$$

This equation finds a far more tractable meaning when one examines the different components of it based upon the time dependence of the terms.

Sum Frequency Generation and Second Harmonic Generation

Sum Frequency Generation (SFG) and Second Harmonic Generation(SHG) are in essence two variations of the same process wherein two photons are parametrically added together resulting in a third photon whose energy is equal to the sum of the first two. SHG is found in Equation 2.13 from the terms

$$P_{SHG} = \epsilon_0 \chi^{(2)} \Big[E_1^2 e^{-2i\omega_1 t} + E_2^2 e^{-2i\omega_2 t} + E_1^{*2} e^{2i\omega_1 t} + E_2^{*2} e^{2i\omega_2 t} \Big]. \tag{2.14}$$

SHG is a special case in which both initial photons are of the same ω, resulting in an emission at 2ω. Two fields are not actually needed for SHG of either ω_1 or ω_2. This arises because the fields inside the pulse are of sufficiently high intensity such that it can interact with itself. This ability to act numerous times with a sample is true generally in nonlinear interactions. SFG, on the other hand, results from the cross terms included in Equation 2.13,

$$P_{SFG} = \epsilon_0 \chi^{(2)} \Big[E_1 E_2 e^{-i(\omega_1+\omega_2)t} + E_1^* E_2^* e^{i(\omega_1+\omega_2)t} \Big]. \tag{2.15}$$

Returning to the last sections derivation of the coupled field equation, the SFG coupled wave equation can be written as

$$\frac{\partial A_{(\omega_1+\omega_2)}(z)}{\partial z} = \frac{2i\epsilon_0 d_{eff}(\omega_1+\omega_2)^2}{\epsilon c^2} A_{\omega_1}(z) A_{\omega_2}(z) e^{i\Big((k_1+k_2-(k_1+k_2)\Big)z}. \tag{2.16}$$

and a SHG polarization of

$$\frac{\partial A_{2\omega_1}(z)}{\partial z} = \frac{2i\epsilon_0 d_{eff}(2\omega)^2}{\epsilon c^2} A_{\omega_1}(z) A_{\omega_1}(z) e^{i(k_1+k_1-2k_1)z}. \tag{2.17}$$

It is important to note that there is no vector or direction in the polarization or in the applied electric field. There are three different types of SFG/SHG that are possible. Type 0 takes two photons of same incident polarization and emits at the same incident polarization. Type I again mixes two photons of the same polarization but the radiated light is emitted at a polarization orthogonal to the propagation and the incident polarization. Type II combines two photons of different polarization and emits at the one of the polarizations which is determined by the medium in which the conversion is happening. The polarization dependence has been included in $\chi^{(n)}$.

Difference Frequency Generation and Optical Parametric Generation

Two photons can be parametrically added to each other in the process of SFG. An alternative process Difference Frequency Generation (DFG), which takes two photons and emits a polarization at energy difference between the two photons energies. This process also arises from the cross terms in Equation 2.13,

$$P_{DFG} = \epsilon_0 \chi^{(2)} \left[E_1^* E_2 e^{-i(\omega_1 - \omega_2)t} + E_1 E_2^* e^{i(\omega_1 - \omega_2)} \right] \tag{2.18}$$

By mathematical analogy, the couple wave equation for DFG is found to be

$$\frac{\partial A_{(\omega_1-\omega_2)}(z)}{\partial z} = \frac{2i\epsilon_0 d_{eff}(\omega_1 - \omega_2)^2}{\epsilon c^2} A_{\omega_1}(z) A^*_{\omega_2}(z) e^{i(k_{\omega_1} - k_{\omega_2} - k_{(\omega_1-\omega_2)})}. \tag{2.19}$$

Like in SHG/SFG, there are Type 0, Type I, and Type 2 DFG. One interesting aspect of DFG is that $A_{(\omega_1-\omega_2)}$ need not have any intensity for this process to start. $A_{(\omega_1-\omega_2)}$ will be produced as a result of the splitting of A_{ω_1} and A_{ω_2}. In this case there will be an exponential generation of the DFG polarization until it is of equal intensity as the two driving fields. This process is known as Optical Parametric Generation (OPG).

2.2.2 Third Order Nonlinear Processes

So far, the only discussed interaction has involved the mixing of two fields in order to produce a polarization. These processes involved $\chi^{(2)}$. Now, situations arising from $\chi^{(3)}$ will be examined.

Self Phase Modulation

Fourier analysis says that a phase applied in the time domain of system results in shift in the frequency domain[35, 34]. Applied generally to some function of time, x(t), this will yield,

$$\mathcal{F}[e^{i\omega_0 t} x(t)] = X(\omega - \omega_0). \tag{2.20}$$

Accordingly, if a temporal phase shift can be applied to the laser pulse propagating through a medium, there will be a generation of new frequencies, the quintessential nonlinear response. Self Phase Modulation (SPM) is a processes where a time domain shift of the phase of a laser pulse is produced as a result of an intensity dependence of the index of refraction. The process receives its name as the intensity of the pulse itself leads to its own phase alteration.

A power series expansion of the index of refraction as a function of intensity can be used as a starting place for describing SPM,

$$n \rightarrow n_0 + n_2(I) + ... \tag{2.21}$$

For this process, a centro-symmetric medium is assumed. For a cento-symmetric medium, the induced polarization should be proportional to the applied electric field. This means that any terms that are proportional to the electric field raised to an even power must vanish, or there would be a physical contradiction as altering the electric field direction would not result in a change of the polarization. As a result, the even terms drop out of the nonlinear polarization term. Further, the series will be truncated for terms higher than $\chi^{(3)}$. This gives the polarization equation

$$P \approx \epsilon_0 \Big[\chi^{(1)} E + \chi^{(3)} E^3 \Big]. \tag{2.22}$$

For this derivation, a driving field of the form

$$E = E_0 cos(kz - \omega t) \tag{2.23}$$

will be used. The resulting polarization is

$$P \approx \epsilon_0 \Big[E_0 \chi^{(1)} cos(\omega t - kz) + E_0^3 \chi^{(3)} cos^3(\omega t - kz) \Big] \tag{2.24}$$

Using the trig identity

$$cos^3(x) = \frac{1}{4}\big(3cos(x) + cos(3x)\big), \tag{2.25}$$

Equation 2.24 reduces to

$$P \approx \epsilon_0 \Big[\chi^{(1)} E_0 cos(\omega t - kz) + \frac{\chi^{(3)} E_0^3}{4} (3cos(\omega t - kz) + cos(3(\omega t - kz) \Big]. \tag{2.26}$$

The cos(3x) term requires phase matching, which will be assumed to not be satisfied. This leaves

$$P \approx \epsilon_0 \Big[\chi^{(1)} E_0 cos(\omega t - kz) + \frac{\chi^{(3)} E_0^3}{4} (cos(\omega t - kz)) \Big] = \epsilon_0 \Big(\chi^{(1)} + \frac{3}{4} \chi^{(3)} E_0^2 \Big) E_0 cos(\omega t - kz). \tag{2.27}$$

The index of refraction must be adjust to be the nonlinear, intensity dependent index of refraction

$$n^2 = 1 + \chi^{(1)} \rightarrow 1 + \chi_{effective} \rightarrow 1 + \Big(\chi^{(1)} + \frac{3\chi^{(3)}}{4} E_0^2 \Big). \tag{2.28}$$

The intensity of an electromagnetic wave is,

$$I = \frac{1}{2} \epsilon_0 c n_0 E_0^2, \tag{2.29}$$

which substitutes into Equation 2.28 to make

$$\chi_{effective} \rightarrow \chi^{(1)} + \frac{3\chi^{(3)}}{4}\frac{2I}{\epsilon_0 n_0 c}. \tag{2.30}$$

Squaring the power series expansion for the index of refraction gives,

$$n^2 = (n_0 + n_2 I + ...)^2 = (n_0^2 + 2n_0 n_2 I + n_2^2 I^2 + ...). \tag{2.31}$$

Reasonably presuming n_2 is small, the n_2^2 term goes to zero. Matching terms from Equation 2.28 yields

$$n_2 = \frac{3}{4}\frac{\chi^{(3)}}{\epsilon_0 n_0^2 c}, \tag{2.32}$$

which is the equation for the intensity dependent index of refraction.

Stepping back to gain some conceptional understanding, the index of refraction, n, is a measure of the bending or slowing of light in a medium. Now, taking the prior derivation into account, the light will bend more if it has a higher intensity. This gives rise to a focusing effect. It is the intensity of the beam that is causing it to a focus onto itself, so this is termed Self Focusing (SF). There is a positive feedback cycle for this process that can lead to even higher order nonlinearities, such as self steepening and space time focusing [35], or destruction of the medium.

Now, with SF in mind, presume an incident ultrafast laser pulse with sufficient intensity such that n_2 becomes relevant. This pulse will have the mathematical form

$$E(z,t) = E_0 e^{-\frac{(t-\frac{z}{v_g})^2}{\tau_0^2}} e^{i\phi(t)}. \tag{2.33}$$

For high intensity light, the intensity dependence of the index of refraction must be considered. This will show up in the system's phase,

$$\phi(t,z) = \omega t - kz \rightarrow \omega t - \frac{\omega}{c}(n_0 + n_2 I)z. \tag{2.34}$$

The frequency of the system is defined as the time derivative of the phase, giving,

$$\frac{\mathrm{d}\phi}{\mathrm{d}t} = \omega + \frac{\omega}{c} n_2 z \frac{\mathrm{d}I}{\mathrm{d}t}. \tag{2.35}$$

Using Equation 2.33 for the intensity and inserting its derivative gives,

$$\frac{\mathrm{d}\phi}{\mathrm{d}t} = \omega - 4\frac{\omega}{c} n_2 z E_0^2 \Big(\frac{t - \frac{z}{v_g}}{\tau_0^2} \Big) e^{\frac{-2(t-\frac{z}{v_g})^2}{\tau_0^2}} \tag{2.36}$$

And so, this system will experience a change in frequency as the beam passes through the medium. This process is known as Self-Phase Modulation. This in the principle effect at play in the process of Super-Continuum Generation (SCG), a method for generating ultra-broadband, octave-spanning spectra which will also be refered to by the term White Light Generation (WLG).

2.2.3 Optical Parametric Amplifier

The results of the last two sections form a basis for understanding an Optical Parametric Amplifier (OPA). In an OPA, a high intensity laser pulse is converted via a series of nonlinear interactions into a high intensity optical field whose frequency and bandwidth can be controlled with phase matching and a temporal delay. These systems are an invaluable component of ultrafast spectroscopy and have a notable role in this thesis.

A typical OPA splits the input beam into two separate beams. One of these beams will generate the high intensity, high photon energy pump. This is accomplished by generating either the second or third harmonic of the pump pulse. A higher

photon energy pump will allow for the amplification of higher energy photons in the continuum, meaning tunability through lower wavelengths of light. The trade-off, however, is that higher order harmonics are generated with a much lower efficiency, resulting in a smaller gain. Fourth harmonic systems have been created, but the strong absorption inside the OPG crystals at short wavelengths makes damage mitigation challenging [37].

The other portion of the input beam will be used for SCG. It is critical that the polarization of the continuum generated be orthogonal to that of the harmonic that is generated. To generate the continuum, the pump beam is focused into a non-centrosymmetric medium, usually a sapphire or Yttrium Aluminum Garnet (YAG) crystal[38, 39, 37]. Inside the crystal, self focusing leads to extremely high intensity fields wherein SPM generates a broad-band continuum. In the case of extremely high intensity pumps, other nonlinear processes can further contribute to the spectral broadening [35, 38, 39, 37]. This light is then dispersed in time so the red wavelengths are preceded by the blue wavelength and the duration of the pulse is several times that of the pump's duration [37]. The output light from the continuum is exceptionally weak, with the SCG usually having an efficiency of around one tenth to a hundredth of a percent.

To increase the intensity of this field, the pump and continuum beams are combined with a dielectric filter and then focused in a DFG crystal in order to perform OPG, which will then amplify the output of the weak continuum exponentially as the beams pass through a crystal. Considering Equation 2.19, the phase matching condition must be satisfied to experience substantial gain. Additionally, the pump field and the chirped white light must be spatially and temporally overlapped to experience gain. A delay stage between the pump and continuum controls the temporal overlap between the colors and can be adjusted

to select a wavelength of amplification. The phase matching condition will vary depending on which portion of the bandwidth of the continuum being amplified. The most basic method for optimizing the bandwidth is to rotate the OPG crystal [35, 38, 39, 37]. The common crystals selected for the mixing are Lithium Triborate (LBO) and beta-Barium Borate (BBO). The continuum will be optimized by selecting a cut along a specific crystal axis chosen by the pump frequency. As both LBO and BBO have a strong birefringence, the phase matching will be optimized if pump and probe are orthogonally polarized[37]. Rotating the crystal will alter the angle of mixing inside the crystal, leading to an increase in gain as a result of minimizing the exponential in Equation 2.19.

A non-colinear arrangement of the beams being focused in the crystals can be used to further satisfy phase matching for more colors inside the continuum bandwidth. This non-colinear OPA is refered to as a NOPA[37]. The increased phase matching in a NOPA results in the amplification of a larger bandwidth of colors. This means that that pulses emitted from a NOPA have a much shorter transform limit than those in a OPA. Even in the non-colinear geometry, it is impossible for the system to amplify the entire bandwidth of a typical continuum, usually around one hundred nanometers, simultaneously with only one pump and continuum beam.

As a result of differences in the index of refraction at the pump and continuum wavelengths, the two pulses will experience temporal walk off as they propagate through the DFG crystal [35, 37]. Once the walk off of the pump is extensive enough, the phase matching angle for the continuum frequencies overlapped with the with pump will no longer be satisfied, meaning no amplification will occur. Additionally, the pump and probe will both experience temporal dispersion from the OPG crystal, stretching them in time. To further amplify the white light, the pump and amplified

beam will be separated and then recombined in a second OPG crystal. If the delay is correct, further amplification will occur. This is known as a multi-stage amplifier[37].

So far, only the amplified portion of the continuum, which is known as the signal, has been discussed. In the generation of the signal, another frequency is also generated. This other portion is known as the idler, and its energy will be the difference between the pump photon energy and the signal photon energy. The idler completes the parametric requirement of the process. This idler is exceptionally useful for long wavelength fields out to Mid-IR [37].

After the signal and idler are generated, the pulses are separated from one another and compressed. To further expand the tunability of these systems, harmonics of the pump and idler can be used to generate signals into the UV. The idler can be used to perform intra-pulse DFG, to generate light well into the Terahertz [37].

Chapter 3

Raman

The Raman effect was discovered by C.V. Raman in 1928 after observing inelastic scattering of sunlight from a medium. He won the Nobel Prize in 1930[40]. In modern optics, the term Raman scattering is used broadly to describe the inelastic scattering of a photon [32] but for the purposes of this thesis, it will be used to specifically describe the inelastic scattering of a visible/near-IR photon from a vibrational mode in a material. For the derivation of all Raman effects, the term vibration will be used, encompassing molecular vibrations and phonons.

3.1 Spontaneous Raman

The most basic implementation of Raman is Spontaneous Raman Spectroscopy (SpRS). In this rather simple experiment, a spectrally narrow pumping field, usually from a laser, excites electrons to a state. In the case of a non-resonant experiment this is a virtual state but it can also be an electronic state, although Resonant Raman effect can occur then [35].

In this excited state, there is a small chance that the electron will interact with a vibrational mode in the material, shifting its energy by the energy of the vibration. When the electron relaxes, it will then emit a photon whose energy has been offset by the vibrational energy. The vibrational energy can either be lost or absorbed. This is known as Stokes or Anti-Stokes scattering. This is depicted in Figure 3.1. The scattered light is collected and the illuminating field is blocked using either a filter or a subtractive monochromator, and the Raman shifted photons are detected by a spectrometer. By measuring the magnitude of the energy shift and utilizing conservation of energy, one can resolve most of a material's vibrational spectrum. Signals for SpRS are weak and acquisition times vary from seconds to minutes, depending on sample cross section.

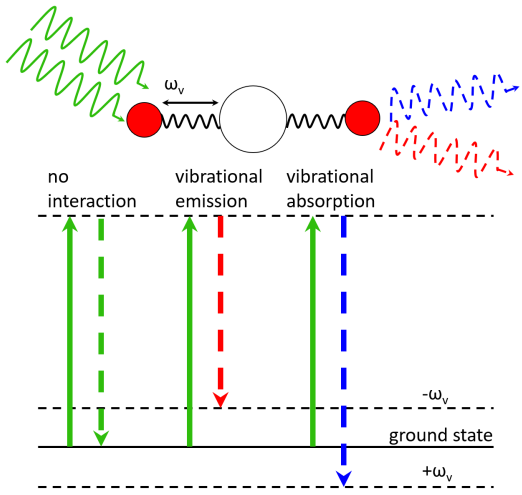

Figure 3.1: Energy diagram depicting Spontaneous Raman scattering. Dashed lines indicate spontaneous emission. Arrow represents nuclear motion

SpRS has found widespread use through a variety of fields. Since the vibrational energies of a material are highly sensitive to composition as well as structure on the order of tens of picometers, Raman spectroscopy has become popular as a non-invasive probe for material fingerprinting, allowing for high precision detection of different lattice and protein structures, molecular isomers, [41] and as well as phase and crystal thickness [27, 42, 22, 29].

3.1.1 Raman basic derivation

A simplistic classical model for Raman scattering can provide substantial insight while remaining quite tractable. One begins with the linear polarization equation,

$$P = \alpha E. \tag{3.1}$$

The effect arises when α is a function of the nuclear coordinate, Q. Taylor expanding around the equilibrium gives

$$\alpha \approx \alpha_0 + \frac{\partial \alpha}{\partial Q} Q + \frac{1}{2} \frac{\partial^2 \alpha}{\partial Q^2} Q^2 + ... = \alpha_0 + \alpha_1 Q + \alpha_2 Q^2 + ... \tag{3.2}$$

The term $\frac{\partial \alpha}{\partial Q}$ represents the change in the polarization of the molecule or solid as a result of a change in nuclear coordinate, which is commonly referred to as the transition dipole moment. An electric field at frequency ω is assumed, as is a sinusoidal change in the nuclear coordinate,

$$E = E_0 cos(\omega t) \quad \text{and} \quad Q = Q_0 cos(\omega_p t). \tag{3.3}$$

This choice of an oscillatory nuclear coordinate is logical as the desired response should be an emitted polarization based on vibrations between atoms in the system. Inserting these into the polarization, results in

$$P = \alpha_0 E_0 + \alpha_1 E_0 Q_0 cos(\omega t) cos(\omega_p). \tag{3.4}$$

A quick trigonometry identity then leads to the solution,

$$P = \alpha_0 E_0 + \alpha_1 E_0 Q_0 \Big(cos\big(\omega - \omega_p)t\big) + cos\big(\omega + \omega_p)t\big) \Big), \tag{3.5}$$

where there is a polarization at both the lower energy Stokes and higher energy anti-Stokes frequency that arises from nuclear motion in the sample. If there is no change in the transition dipole moment upon excitation the system will not experience a Raman shift. This means that Raman does not effectively probe all vibrational modes in a material as some vibrations do not induce a change in the dipole moment and further does not work on metals, where the free electrons oscillate to prevent any form of dipole forming.

3.1.2 Spontaneous Raman Thermometry

Raman spectroscopy can provide a direct measure of the temperature of a system [34, 35, 43]. During the inelastic interaction, a vibration can be not only emitted, but also absorbed. Vibration absorption occurs according to the number of vibration in the material, which is directly related to the temperature of the sample. Vibration emission will occur at a rate independent of the temperature.

This can be demonstrated mathematically with some ease[44]. Beginning with the probability of an emission based on a Boltzmann distribution,

$$\mathcal{P} = \frac{e^{\frac{-\hbar\omega_v}{k_b T}}}{\mathcal{Z}}, \tag{3.6}$$

where $\hbar$ is Planck's constant, $\mathcal{Z}$ is the partition function, ω_v is the vibrational energy, and k_b is Boltzmann's constant. If the Stokes energy is taken to be the ground state energy and the Anti-Stokes is taken to be the first excited state, the probability of the Anti-Stokes divided by the Stokes is

$$\frac{\mathcal{P}_{AS}}{\mathcal{P}_S} = e^{\frac{-\hbar\omega_v}{k_b T}}. \tag{3.7}$$

Experimentally measuring probabilities can be challenging. It is far more simple to measure spectral intensities. These intensities must also take into account the scattering efficiencies at the different wavelengths, which are proportional to the wavelength of the light being scattered to the fourth power [45]. This leads to

$$\frac{I_{AS}}{I_S} = \frac{(\omega_L + \omega_v)^4}{(\omega_L - \omega_v)^4} e^{\frac{-\hbar\omega_v}{k_b T}} = \frac{\omega_{AS}^4}{\omega_S^4} e^{\frac{-\hbar\omega_v}{k_b T}}, \tag{3.8}$$

where the illumination source has a frequency of ω_L. Experiments utilizing this technique is known as Raman thermometry [46].

3.2 Stimulated Raman Scattering

While SpRS has a tremendous capability to identify materials and study vibrational modes, it does have several shortcomings. The first problem is the weak signal, with roughly one out of every million or so photons incident on the sample. A method for increasing the efficiency of Raman is to perform Stimulated Raman Spectroscopy (SRS). With this technique, an additional field is applied to the sample in order to drive the transition to the vibrational mode. Typical enhancement factors vary between 10^6 and 10^8 [47].

Two intuitive pictures for SRS exist. In the first, in a direct comparison to SpRS, a pumping field excites electrons to a virtual or electronic state. This field must then be overlapped with a stimulating field, whose frequency will be scanned over a range. If the difference in energy between the two fields' energy is equal to a vibrational energy in the sample, stimulated emission will occur, resulting in conversion of photons from the pumping field into the stimulating field, as seen in Figure 3.2. An alternative perspective of this process arises by realizing that the overlap of two laser pulses will

beat at the difference of their frequencies. When the difference of the frequencies is equal to a vibrational frequency, the beating of the two fields will drive vibrations in the material, resulting in a higher chance of interaction between the excited electrons and the vibrational modes. Both perspectives are valid and by measuring the gain on the stimulating field as a function of frequency with a power meter or photodiode, one can resolve the vibrational spectrum of the sample.

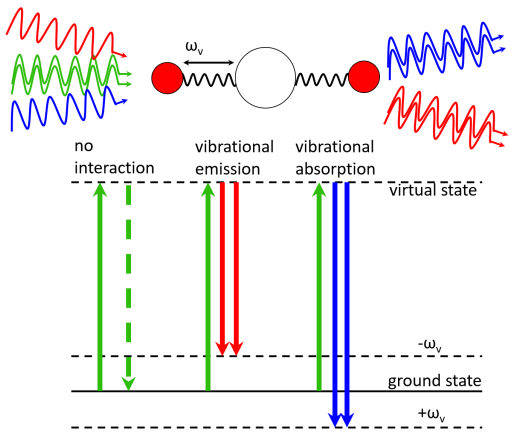

Figure 3.2: Image depicting Stimulated Raman. Solid lines indicate stimulated emission. Arrow represents nuclear motion

The main downsides of SRS are shared with SpRS, mainly the inability to probe materials without a transition dipole moment and the absence of temporal resolution. Modes without an induced transition dipole moment can be studied using infrared spectroscopy, which is beyond the scope of this thesis. The absence of temporal resolution makes it is exceptionally challenging or impossible to resolve vibrational dynamics on their fundamental time scales. A large amount of effort has been dedicated to developing time resolved techniques for SRS, such as Coherent Anti-Stokes Raman Scattering (CARS) [35], Coherent Stokes Raman Scattering (CSRS)[48], and Femtosecond Stimulated Raman Scattering (FSRS)[10, 4, 1], the last of which I will discuss in Section 5.

An excellent theoretical model for SRS begins by tracking the nuclear coordinate in a material. Its motion is assumed to be of the form of a damped driven harmonic oscillator,

$$\frac{\mathrm{d}^2\bar{q}}{\mathrm{d}t^2} + 2\gamma\frac{\mathrm{d}\bar{q}}{\mathrm{d}t} + \omega_p^2\bar{q} = \frac{F(t)}{m}, \tag{3.9}$$

where $\bar{q}$ is the nuclear coordinate, γ is the vibrational lifetime, ω_p is the vibrational lifetime, and $F(t)$ is the driving force, and m is the mass of the atom. It will also be assumed that the applied electric field will be providing the driving force in this situation and will induce a dipole in the medium. The energy to construct such a dipole is given by

$$W = \frac{1}{2}\langle\bar{p}(z,t)\cdot\bar{E}(z,t)\rangle = \frac{1}{2}\epsilon_0\alpha\langle\bar{E}^2\rangle, \tag{3.10}$$

and that to find the force on the system, a derivative of the spatial coordinate, q, is taken

$$F(t) = \frac{\mathrm{d}W}{\mathrm{d}q} = \frac{\epsilon_0}{2}\Big(\frac{\partial\alpha}{\partial q}\Big)_0\langle\bar{E}^2\rangle. \tag{3.11}$$

This will be the form of the force on the damped harmonic oscillator. In the case of SRS, there are two electric fields present. The illuminating field will be from a narrow-linewidth laser with an intensity of A_L, frequency and wave-vectors ω_L and k_L respectively. The other beam, which will be referred to as the Stokes field, will have amplitude A_S with associated ω_S and k_L. This is expressed mathematically as,

$$E(z,t) = \left(A_L e^{i(k_L z-\omega_L t)} + A_S e^{i(k_S z-\omega_S t)} + A_L^* e^{-i(k_L z-\omega_L t)} + A_S^* e^{-i(k_S z-\omega_S t)}\right). \tag{3.12}$$

Inserting this into Equation 3.11, results in

$$\begin{aligned}\bar{F}(t) =& \frac{\epsilon_0}{2}\Big(\frac{\partial\alpha}{\partial q}\Big)_0\Big[A_L A_L e^{2i(k_L z-\omega_L t)} + A_S A_S e^{2i(k_S z-\omega_S t)} + A_L^* A_L^* e^{-2i(k_L z-\omega_L t)} \\ &+ A_S^* A_S^* e^{-2i(k_S z-\omega_S t)} + 2|A_L|^2 + 2|A_S|^2 + 2A_L A_S e^{i\left((k_L+k_S)z+(\omega_L+\omega_S)t\right)} \\ &+ 2A_L^* A_S^* e^{-i\left((k_L+k_S)z+(\omega_L+\omega_S)t\right)} + 2A_L A_S^* e^{i\left((k_L-k_S)z+(\omega_L-\omega_S)t\right)} \\ &+ 2A_L^* A_S e^{-i\left((k_L-k_S)z+(\omega_L-\omega_S)t\right)}\Big]\end{aligned} \tag{3.13}$$

The components of the force that are oscillating at the difference between stokes frequency and light frequency are taken. These are

$$F(t) = \epsilon_0\Big(\frac{\partial\alpha}{\partial q}\Big)_0\Big[A_L A_S^* e^{i\left((k_L-k_S)z-(\omega_L-\omega_S)t\right)} + A_L^* A_S e^{-i\left((k_L-k_S)z-(\omega_L-\omega_S)t\right)}\Big]. \tag{3.14}$$

The superposition of two beams of different frequency will beat at the difference frequency between the two beams. In SRS, this beating coherently drives a vibrational mode in the system, which is responsible for the stimulated emission. With these ideas in mind, solutions are sought where the position of the molecule or lattice moves in sync with the beating fields,

$$\bar{q} = q(\omega_L-\omega_S)e^{i\left((k_L-k_S)z-(\omega_L-\omega_S)t\right)} + q^*(\omega_L-\omega_S)e^{-i\left((k_L-k_S)z-(\omega_L-\omega_S)t\right)}. \tag{3.15}$$

As conjugation is a linear process, only the non-conjugate term is solved here, and then it is conjugated and added to construct the final answer. Inserting Equations 3.14 and 3.15 into Equation 3.9 and canceling out the time dependence yields

$$-(\omega_L-\omega_S)^2 q(\omega_L-\omega_S) - i\gamma(\omega_L-\omega_S)q(\omega_L-\omega_S) + \omega_p^2 q(\omega_L-\omega_S) = \epsilon_0\Big(\frac{\partial\alpha}{\partial q}\Big)_0[A_L A_S^*]. \tag{3.16}$$

solving for q gives

$$q(\omega_L-\omega_S) = \frac{\frac{\epsilon_0}{m}A_L A_S^*\Big(\frac{\partial\alpha}{\partial q}\Big)_0}{\Big(\omega_p^2-(\omega_L-\omega_S)^2 - i\gamma(\omega_L-\omega_S)\Big)}, \tag{3.17}$$

which is used to find $\bar{q}$

$$\begin{aligned}\bar{q}(\omega_L-\omega_S) &= q(\omega_L-\omega_S)e^{i\left((k_L-k_S)z-(\omega_L-\omega_S)t\right)} + q^*(\omega_L-\omega_S)e^{-i\left((k_L-k_S)z-(\omega_L-\omega_S)t\right)} \\ &= \frac{\frac{\epsilon_0}{m}A_L A_S^*\Big(\frac{\partial\alpha}{\partial q}\Big)_0}{\Big(\omega_p^2-(\omega_L-\omega_S)^2 - i\gamma(\omega_L-\omega_S)\Big)}e^{i\left((k_L-k_S)z-(\omega_L-\omega_S)t\right)} \\ &+ \frac{\frac{\epsilon_0}{m}A_L^* A_S\Big(\frac{\partial q}{\partial\alpha}\Big)_0}{\Big(\omega_p^2-(\omega_L-\omega_S)^2 + i\gamma(\omega_L-\omega_S)\Big)}e^{-i\left((k_L-k_S)z-(\omega_L-\omega_S)t\right)}\end{aligned} \tag{3.18}$$

Inside the polarization there is a complex Lorentzian amplitude that is propagating at the vibrational frequency. Inserting Equations 3.18 and 3.12 into the polarization, Equation 3.4, that has been expanded in terms of the nuclear coordinate,

$$P = \epsilon_0\alpha E \approx \epsilon_0\big(\alpha_0 + \Big(\frac{\partial\alpha}{\partial q}\Big)_0\bar{q}\big)E. \tag{3.19}$$

Only the response from the perturbed nuclear coordinate is taken, resulting in,

$$\bar{P}_{NL} = \frac{\epsilon_0 \left(\frac{\partial \alpha}{\partial q}\right)_0}{m} \left(\frac{\epsilon_0 A_L A_S^* \left(\frac{\partial \alpha}{\partial q}\right)_0}{\left(\omega_p^2 - (\omega_L - \omega_S)^2 - i\gamma(\omega_L - \omega_S)\right)} e^{i\left(k_L - k_S)z - (\omega_L - \omega_S)t\right)} \right.$$
$$\left. + \frac{\epsilon_0 A_L^* A_S \left(\frac{\partial \alpha}{\partial q}\right)_0}{\left(\omega_p^2 - (\omega_L - \omega_S)^2 + i\gamma(\omega_L - \omega_S)\right)} e^{-i\left(k_L - k_S)z - (\omega_L - \omega_S)t\right)} \right) \tag{3.20}$$
$$* \left(A_L e^{i(k_L z - \omega_L t)} + A_S e^{i(k_S z - \omega_S t)} + A_L^* e^{-i(k_L z - \omega_L t)} + A_S^* e^{-i(k_S z - \omega_S t)} \right),$$

which expands into a cumbersome but rich equation for the polarization,

$$
\begin{aligned}
\bar{P}_{NL} = & \frac{\frac{\epsilon_0^2}{m} A_L A_S^* A_L \left(\frac{\partial \alpha}{\partial q}\right)_0^2}{\left(\omega_p^2 - (\omega_L - \omega_S)^2 - i\gamma(\omega_L - \omega_S)\right)} e^{i\left(2k_L - k_S)z - (2\omega_L - \omega_S)t\right)} \\
& + \frac{\frac{\epsilon_0^2}{m} A_L^* A_L A_S \left(\frac{\partial \alpha}{\partial q}\right)_0^2}{\left(\omega_p^2 - (\omega_L - \omega_S)^2 + i\gamma(\omega_L - \omega_S)\right)} e^{i(k_S z - \omega_S t)} \\
& + \frac{\frac{\epsilon_0^2}{m} A_L A_S A_S^* \left(\frac{\partial \alpha}{\partial q}\right)_0^2}{\left(\omega_p^2 - (\omega_L - \omega_S)^2 - i\gamma(\omega_L - \omega_S)\right)} e^{i(k_L z - \omega_L t)} \\
& + \frac{\frac{\epsilon_0^2}{m} A_L^* A_S A_S \left(\frac{\partial \alpha}{\partial q}\right)_0^2}{\left(\omega_p^2 - (\omega_L - \omega_S)^2 + i\gamma(\omega_L - \omega_S)\right)} e^{-i\left(k_L - 2k_S)z - (\omega_L - 2\omega_S)t\right)} \\
& + \frac{\frac{\epsilon_0^2}{m} A_L A_S^* A_L^* \left(\frac{\partial \alpha}{\partial q}\right)_0^2}{\left(\omega_p^2 - (\omega_L - \omega_S)^2 - i\gamma(\omega_L - \omega_S)\right)} e^{-i(k_S z - \omega_S t)} \\
& + \frac{\frac{\epsilon_0^2}{m} A_L^* A_L^* A_S \left(\frac{\partial \alpha}{\partial q}\right)_0^2}{\left(\omega_p^2 - (\omega_L - \omega_S)^2 + i\gamma(\omega_L - \omega_S)\right)} e^{-i\left(2k_L - k_S)z - (2\omega_L - \omega_S)t\right)} \\
& + \frac{\frac{\epsilon_0^2}{m} A_L A_S^* A_S^* \left(\frac{\partial \alpha}{\partial q}\right)_0^2}{\left(\omega_p^2 - (\omega_L - \omega_S)^2 - i\gamma(\omega_L - \omega_S)\right)} e^{i\left(k_L - 2k_S)z - (\omega_L - 2\omega_S)t\right)} \\
& + \frac{\frac{\epsilon_0^2}{m} A_L^* A_S^* A_S \left(\frac{\partial \alpha}{\partial q}\right)_0^2}{\left(\omega_p^2 - (\omega_L - \omega_S)^2 + i\gamma(\omega_L - \omega_S)\right)} e^{-i(k_L z - \omega_L t)}.
\end{aligned}
\tag{3.21}
$$

From this equation, there are several contributions that are worth noting. Of primary interest are the contributions from the that are emitted at the frequency of the stimulating beam,

$$
\bar{P}_S = \frac{\frac{\epsilon_0^2}{m} A_L^* A_L A_S \left(\frac{\partial \alpha}{\partial q} q\right)_0^2}{\left(\omega_p^2 - (\omega_L - \omega_S)^2 + i\gamma(\omega_L - \omega_S)\right)} e^{i(k_S z - \omega_S t)} + \frac{\frac{\epsilon_0^2}{m} A_L A_S^* A_L^* \left(\frac{\partial \alpha}{\partial q}\right)_0^2}{\left(\omega_p^2 - (\omega_L - \omega_S)^2 - i\gamma(\omega_L - \omega_S)\right)} e^{-i(k_S z - \omega_S t)}. \tag{3.22}
$$

Following from the coupled wave system, both of the contributions in Equation 3.22 will be transforming energy from the illuminating field and into the Stokes field. This conversion from pump to Stokes field is why the SRS signal is always measured as gain. Additionally, it is worth noting that the emitted field always follows the direction of the Stokes beam and additionally that the phase matching condition is satisfied innately [35, 34]. This result can also be used to explain why SRS has a substantially stronger signal than in SpRS. In SpRS, the terms A_S and A_S^* arise through exceptionally weak vacuum fluctuations. As a result of the intensity of this specific field being very weak, the emitted polarization is substantially weaker[49, 33].

Remember also that ω_S is a variable and it can be greater or smaller than ω_A. In the case that $\omega_S < \omega_A$, when ω_S aligns with a vibrational energy level, there is a negative dampening as $\omega_L - \omega_S$, leading to a gain in the field A_S.

Fruitful results are also be obtained by examining the relationship between the Stokes and Anti-Stokes frequencies,

$$\omega_L - \omega_S = -(\omega_L - \omega_{AS}), \tag{3.23}$$

which can be rearrange to see

$$\omega_{AS} = 2\omega_L - \omega_S. \tag{3.24}$$

If instead $\omega_S = 2\omega_A - \omega_S = \omega_{AS}$ in Equation 3.22 a depletion effect of that field will be observed. This response is commonly described as Inverse Raman Scattering (IRS), as it will show up as a depletion blue shifted from the pump field. As depletion requires some field already present to be depleted, this signal response will only be visible in certain circumstances.

It is worth noting that this different spectral contribution still arises from the same polarization equation. The reason for this lies in the fact that there are numerous ways in which the three fields A_L, A_L^* and A_S can be arranged, which relate to different quantum pathways. This will be highly relevant to the discussion of Femtosecond Stimulated Raman Spectroscopy later.

The relationship found in Equation 3.24 also arises in the nonlinear polarization that seen before, Equation 3.21. While some authors attribute this to a general four wave-mixing, it is far more intuitive in this instance to define it according to Equation 3.24 as an Anti-Stokes scattering term. Substituting Equation 3.24 yields,

$$\begin{aligned}
\bar{P}_{AS} &= \frac{\frac{\epsilon_0^2}{m} A_L A_S^* A_L \left(\frac{\partial \alpha}{\partial q}\right)_0^2}{\left(\omega_p^2 - (\omega_L - \omega_S)^2 - i\gamma(\omega_L - \omega_S)\right)} e^{i\left(2k_L - k_S)z - (2\omega_L - \omega_S)t\right)} \\
&+ \frac{\frac{\epsilon_0^2}{m} A_L^* A_L^* A_S \left(\frac{\partial \alpha}{\partial q} q\right)_0^2}{\left(\omega_p^2 - (\omega_L - \omega_S)^2 + i\gamma(\omega_L - \omega_S)\right)} e^{-i\left(2k_L - k_S)z - (2\omega_L - \omega_S)t\right)} \\
&= \frac{\frac{\epsilon_0^2}{m} A_L A_S^* A_L \left(\frac{\partial \alpha}{\partial q}\right)_0^2}{\left(\omega_p^2 - (\omega_L - \omega_{AS})^2 + i\gamma(\omega_L - \omega_{AS})\right)} e^{i(k_{AS} z - \omega_{AS} t)} \\
&+ \frac{\frac{\epsilon_0^2}{m} A_L^* A_L^* A_S \left(\frac{\partial \alpha}{\partial q}\right)_0^2}{\left(\omega_p^2 + (\omega_L - \omega_{AS})^2 + i\gamma(\omega_L - \omega_{AS})\right)} e^{-i(k_{AS} z - \omega_{AS} t)}
\end{aligned} \tag{3.25}$$

From this equation, a different response to that seen in Equation 3.22 is obtained. Here, there is no longer have a self satisfied phase matching relationship. This means that this term will not be satisfied simultaneously as in Equation 3.22. Additionally, this term will take fields as ω_L and ω_S and emit a signal at the blue shifted ω_{AS}. The gain and depletion effect here is reversed in the Anti-Stokes scattering term, so pumping at ω_S produces a gain at ω_{AS}. This, it turns out, is the quantum pathway that is probed in Coherent Anti-Stokes Raman Spectroscopy [48], an alternative ultrafast Raman technique to FSRS.

Chapter 4

2D Materials

2D materials were first hypothesized during the rise of the quantum theory of condensed matter in the 1940's [50]. Although numerous reports were made prior, the true isolation of single and few layer atomically thin crystals was not realized until 2004, when Andre Geim and Konstantine Novosolev successfully isolated graphene using the mechanical exfoliation technique, more colloquially known as the "Scotch Tape" method [17]. Since then, numerous other 2D materials have been isolated and studied in immense detail, with properties ranging from insulators, to super conductors [51], to semi-metals[18, 24, 52]. The recent discovery of magnetic 2D materials has opened up even further avenues of research [53, 54].

2D materials have attracted widespread interest among researchers for not only their unique quantum confinement but additionally for their application to technology [24, 28]. As a result of the single to few layer out of plane confinement, these systems boast many unique properties ranging from the Massless Dirac Fermions present in graphene [20] to the layer dependent photoluminescence seen in MoS_2 [18]. The technological benefits from even a mostly complete understanding of these systems are widespread. In the ongoing quest to produce ultra-scaled electronic devices, the

atomic scale, .3 to .8 nm [17], boasted by 2D materials presents a tantalizing option for producing exceptionally thin devices. Additionally, the absence of any out of plane bonds means they can be stabley stacked on top of other without the dislocations experienced by more traditional bulk materials [26, 24]. This makes 2D materials ideal for the construction of heterostructures. These systems are created by stacking numerous layers of different 2D materials on top of each other. There are many knobs that can be utilized to fine tune the electronic and thermal structure of such a 2D material heterostructure as their properties can be drastically altered based upon the number of layers, the types of materials within the layers, and the geometric arrangement of the layers [25].

4.1 Mechanical Exfoliation

Mechanical exfoliation provides an experimentally simple method for acquiring 2D materials[17], although the intricacies of it are nuanced, and the work of many PhD's. From a basic standpoint, the process is exceptionally simple. The starting point is a bulk crystal consisting of millions of layers of 2D crystals stacked on top of each other. This bulk crystal is placed on a piece of tape and by sticking the tape together and peeling it apart repeatedly, the sheets will be cleaved from one another until there are just a few layers stacked. This piece of tape is then set on a substrate and removed, and as there is no bond between the sheet or the crystal, a monolayer or few layer crystal will hopefully be deposited on the sample.

Although this might sound like a trivial process, the finesse required for repeatable high quality exfolation and observation can be challenging. A perfect example of this subtlety is the choice of substrate. A .3 nm thick 2D crystal creates a nearly nonexistent optical contrast to whatever substrate it is deposited on, making it

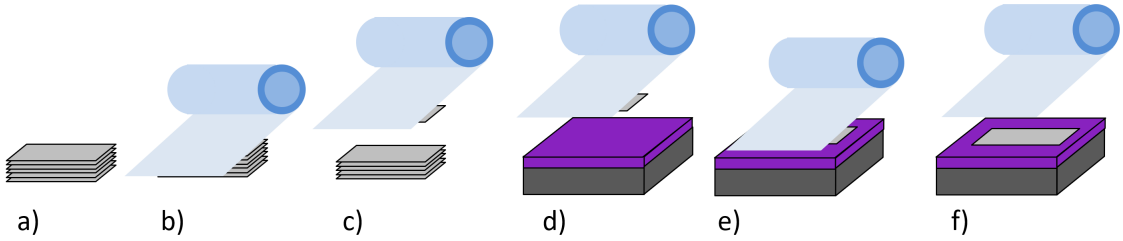

Figure 4.1: Step by step representation of the mechanical exfoliation process.

challenging to locate. In order to optimize this contrast, one must carefully select a specific silicon oxide thickness on a Si substrate in order to easily see the sample. In the case of .3 nm graphene, this thickness is 90 nm. For .6 nm MoS_2, either a 285 nm or 300 nm oxide will optimize the contrast. Historically, this was a critical step in isolating these 2D materials [17].

4.2 Exfoliation Procedure

Exfoliation starts with a round silicon wafer, one with an appropriately thick oxide layer for whatever material is being exfoliated. The wafer is placed with the polished side up onto a Kimtec wipe. While wearing gloves, use a stainless steel razor and a diamond scribe to make a scratch 4 mm to 10 mm from the side and perpendicular to the flat end of the wafer. The flat side is used to demarcate the crystal axis and perpendicular to this flat side cleaves easiest. Using the wafer and a razor, fracture the wafer along the scribed line and the edge. Next, take that long and narrow slice of wafer and using the razor and scribe, divide it into rectangles with sides of 4 mm to 7 mm.

Cleanliness is a key aspect of the exfoliation process. Any debris on the substrate or sample reduces the contact area between the two. As the only out of plane forces

in these materials are Van der Waals interactions, which drop off over extremely short distances, any obstruction to a clean contact will greatly reduce the efficiency of the exfoliation. Accordingly, the wafer is cleaned with Acetone, Isopropanol, and then Methanol, in that order, using the following process. Fill a well cleaned 100 mL beaker with 10 mL to 20 mL of solvent and then sonicate it for 5 minutes. Using tweezers, remove the diced wafer pieces one at a time and quickly blow off the solvent using either compressed air or nitrogen. If a large amount of residue is visible on the wafer, place it back into the solvent and repeat. After this round of solvents, it is ideal to use an acidic Piranha solution, a combination of hydrogen peroxide and sulfuric acid, or oxygen plasma ablation to clean the wafer, however it is not necessary if they are not easily available. This finishes the preparation of the substrate.

High quality mechanical exfoliation works best with bulk samples that have large crystal domains in them. Some of the bulk crystals were provided in part by our collaborator, Dr. Samuel Berweger, at the National Institute of Standards and Technology and others were purchased from 2dsemiconductors. Typical parent crystals are a few millimeters in scale. Using tweezers, remove a small portion of material from the parent crystal. The scale of the portion removed from the parent crystal can vary, but a fleck that is less than half a millimeter will be more than enough.

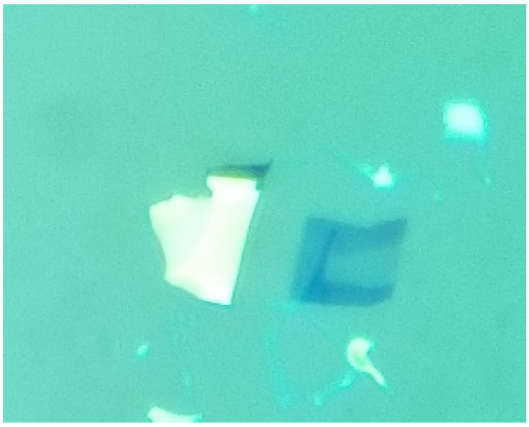

Figure 4.2: Optical microscope image of a mono- to few- layer sample of exfoliated graphene. The yellow crystal is a bulk structure. Shades of lighter purple are fewer layer samples of graphene with the lightly colored center being a monolayer area.

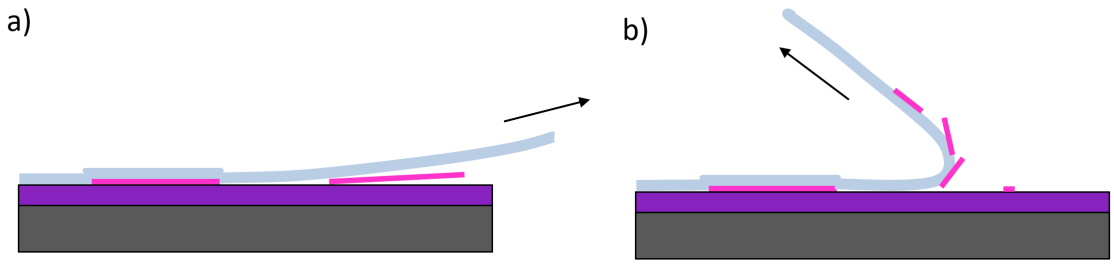

Figure 4.3: a) Proper and b) improper way to pull apart tape during exfoliation. The light blue line represents the dicing tape and the pink lines are crystals. The purple and grey areas represent the oxide layer and the silicon wafer. The slow pulling at low angle seen in a) applies generally to the process. Arrows indicate the direction of the force. The low angle in a) prevents the damage seen in b) and smoothly deposits the sample onto the substrate.

Place the fleck onto the dicing tape. The advantage of dicing tape is that that it usually does not leave residue after it has been applied to a surface, making it ideal for cleaving the adjacent layers without polluting the sample with polymers. However, when creased, the adhesive in the tape can actually fracture and be deposited onto the substrate while simultaneously reducing the efficiency of the exfoliation of the 2D material. Accordingly, great care should be taken to prevent any creasing or unnecessary folding. Further, extreme care should be taken to not to touch the adhesive side of the dicing tape. This will pollute samples and diminish the mono-layer yield.

To cleave the layers from the bulk, one must gently place the tape onto itself, sandwiching the crystal between the two sides of the tape. Run a finger gently over the area where the crystal is located. Next pull the tape from itself, taking special attention to try to pull at a low angle with high tension, as shown in Figure 4.3.

Pulling the tape apart from itself at a right angle or greater can lead to fracturing of the adhesive and should be avoided. Further, the bending of the tape is less likely

to "set" a monolayer sample onto the substrate and more likely to break the crystal and leave it attached to the tape.

The number of times that the tape should be placed on itself and removed should be determined based on the size of the sample needed and the cost. Fewer iterations of this process will result in larger mono- and few- layer crystals on the samples.

This can lead to a lot of substrates and bulk crystal use, which is more expensive. More iterations will have a higher chance of exfoliation but smaller domain sizes.

After the desired number of iterations with the dicing tape, one then takes Scotch Magic Tape or Transparent Tape, and places it on top of the dicing tape so the adhesive sides are touching each other with the crystal in between. After running a finger along the tape, slowly pull the tapes apart from each other, trying to keep the angle between the tapes as small as possible and trying to keep high tension on the tape. Once the Scotch tape has been removed from the dicing tape, place the cleaned substrates polished side up onto the adhesive side of the Scotch tape. Let the substrate settle over night.

The final step is to remove the substrate from the tape. While doing this, make certain to once again keep the angle between the tape and substrate as shallow as possible and to pull slowly with high tension. After removing the substrate from the tape, use an optical microscope to inspect the sample for mono- and few- layer crystals that have been deposited on the substrate.

4.3 Exfoliated samples and characterization

Mechanical exfoliation of mono- and few- layer 2D materials was achieved for graphene, MoS_2, $MoTe_2$, and ReS_2. Optical images of the samples of graphene as well as ReS_2 can be seen in Figure 4.2 and 4.5 respectively. Although exact scale

characterization was not possible due to resolution problems on the atomic force microscope available in the physics building, most mono- to few- layer samples are believed to be on the scale of tens of micrometers. The weak optical contrast is highlighted in Figure 4.2.

In order to verify the quality and nature of the samples produced, it was necessary to characterize them using SpRS. As mentioned in Section 3.1, SpRS is highly sensitive to structure and is one of the few probes capable of distinguishing mono-layer and few-layer crystals from one another. Figure 4.4 shows a schematic of the simple SpRS apparatus that was built for for sample characterization during this project. A 532 nm diode laser and a 633 nm Helium Neon (HeNe) laser are used for pump beams. A magnetic mirror mount can be used to swap between light sources. The desired beam passes through a 50/50 beam splitter is focused onto a sample with a 20x microscope objective.

The sample is mounted on a three axis translational stage to navigate laterally on the sample and to bring the sample into the focus of the beam. To aid in sample imaging and for navigation, an LED light source has been coupled into the objective with the help of a high transmission beam splitter. As the LED has a high power output, the high transmission was chosen to reduce the amount of pump beam and signal deflected. After the image has reflected off of the 50/50 beam splitter, it is sent to a camera that is connected to a computer

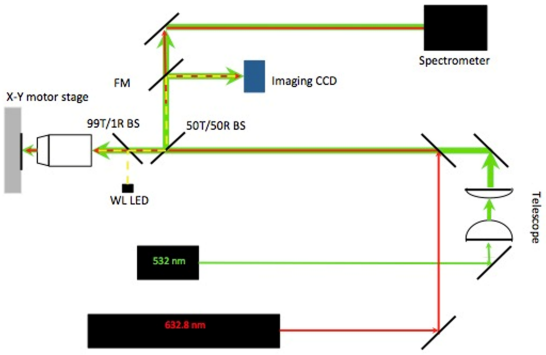

Figure 4.4: Schematic form SpRS setup. FM is flipe mirror. WL is white light. BS is beam splitter.

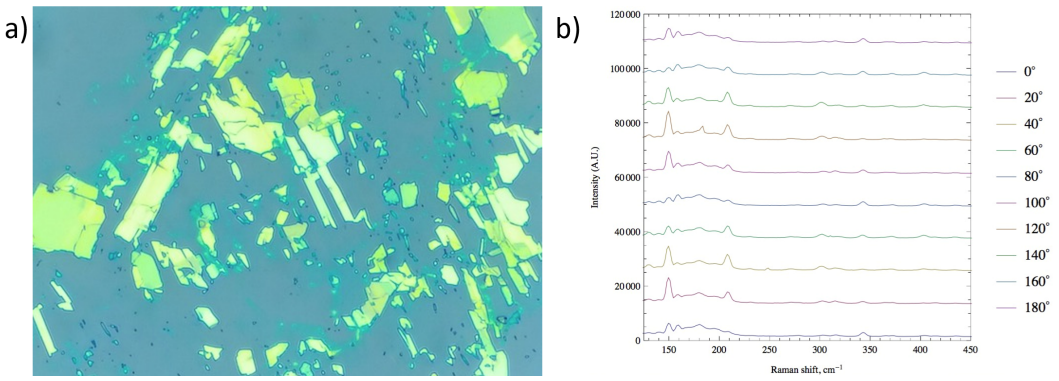

Figure 4.5: a) Optical image of a mechanically exfoliated ReS_2 sample and b) corresponding polarization dependent Raman spectra. The angles on the right are measured on a half wave plate, which is rotated to adjust the polarization of the incident beam. Results compare to [55].

for easy viewing. After a specific crystal has been found on the sample, the LED can be turned off, leaving only the pump laser focused onto the sample. The objective also doubles as a collection optic for the scattered light. The signal is reflected off of the beam splitter and directed into an imaging spectrometer for detection.

Figure 4.5 shows the Polarization dependent Raman spectra seen in ReS_2. This feature arises as the result of geometrically linear interactions chains of Re atoms forming in the lattice [55]. When samples have large domains, these chains result in an altered Raman response when the light is polarized parallel them. This effect is clearly seen in Figure 4.5, indicating high quality ReS_2 exfoliatons.

4.4 Exfoliated Sample Summary

The Siemen's lab now has all of the materials necessary for the fabrication of mechanically exfoliated samples. The exfoliation process has been described in great detail in the last section of this thesis. An overarching theme through the process is to prevent sample contamination from either external sources, such as oils on hands

or dust from the air, as well as from the adhesives used during the exfoliation. Pulling the tape apart at low angles with high tension optimizes the success rate of achieving mono- and few- layer samples. Samples of mono- to few- layer Graphene, MoS_2, $MoTe_2$, and ReS_2 were made.

Sample characterization can easily be achieved with the SpRS setup. Since the writing of this thesis, the experiment has also been augmented with a 450 nm illumination source to perform photoluminescence measurements as well.

A future improvement in the lab's capabilities is to create a sample transfer process. A controlled method of moving crystals from one substrate to another can be used to construct heterostructures.

Chapter 5

Femtosecond Stimulated Raman Spectroscopy

A major drawback of SpRS and SRS is their inability to acquire information about sample dynamics. Several techniques have been developed to acquire vibrational dynamics. Femtosecond Stimulated Raman Spectroscopy (FSRS), can resolve vibrational dynamics with femtosecond resolution.

In a FSRS experiment, two distinct laser pulses are required; a narrow bandwidth picosecond pulse to excite a population of electrons as well as a broadband, femtosecond laser pulse to

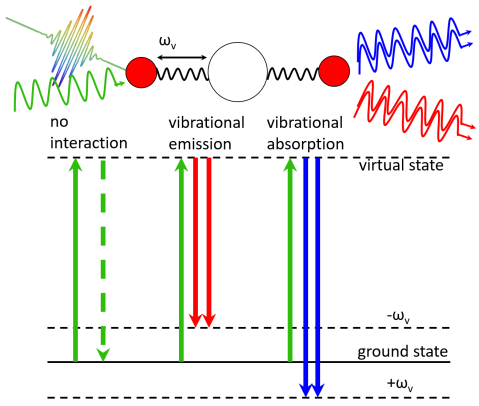

Figure 5.1: Energy level diagram of the FSRS process. It is similar to SRS, however, a broadband pulse drives stimulated emission at numerous vibrational frequencies simultaneously.

drive stimulated emission at the vibrationally shifted frequencies within the pulse's bandwidth. This is in contrast to SRS, where two picosecond pulses are overlapped and one's frequency must be tuned through a range until conversion from the pump to the probe beam is observed.

This reveals the two-fold benefit of FSRS over SRS. First, a frequency tunable laser is not needed, simplifying the apparatus and data collection. Deeper inspection shows that, as a result of the nonlinearity required for SRS to occur, there will not be a FSRS signal except when both the pump and probe pulses are overlapped [47]. Because the probe pulse has a duration on the order of tens of femtoseconds, the FSRS spectra contain vibrational snapshots with a window on scale of tens of femtoseconds [1].

It is then possible to bring a third pulse into the sequence, an actinic pump, that will induce some dynamics in the system. By altering the time delay between the actinic pump and the Raman pulses, vibrational dynamics with exceptional temporal and spectral resolution can be observed. This is depicted in Figure 5.2 In such a setup, FSRS can resolve dynamic vibrational spectra on ultrafast time scales.

FSRS was first implemented in the late 1990's by Yoshizawa [10]. This first implementation showed gain at vibrational energies on a femtosecond pulse spectum as a result of temporal overlap with a picosecond pulse, but the signal to noise ratios were poor and the spectral resolution was worse than the result of the picosecond pulse alone. FSRS was matured in the following years

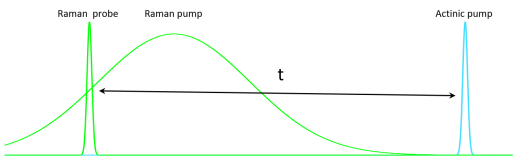

Figure 5.2: Pulse sequence for a FSRS pump-probe experiment. t represents the time delay between the initiation of the dynamics and the time when the system's structure would be probed.

by Matthies, where regenerative amplified laser systems lead to high enough signal that single pulse readouts of spectrum were capable of being detected on USB spectrometers. This same group also developed a full quantum mechanical description of FSRS [6]. Over the past decade, FSRS has matured and branched into applications in imaging in biological systems [56, 57, 33] and performing ultrafast thermometry [58, 59].

FSRS has long history of revealing molecular reaction dynamics [4, 11, 2], solavation interaction [60], and foldings of large molecules like proteins [61, 3]. There are several reasons that FSRS works exceptionally well with these liquid samples. For one, liquids are often less prone to damage from the high intensity FSRS pump pulse as the energy of the pulse is distributed over an large number of emitters. This problem can be further mitigated as fluid samples can be probed as jets, in which samples are streamed through the beam path and replenished after they are thermally ablated. However, vibrational dynamics in other materials science systems such as 2d materials could strongly benefit from the high spectral and temporal resolution achieved by FSRS.

5.1 FSRS quantum paths

As discussed in Section 2.1.2, it is highly useful to examine the quantum pathways that are present in a nonlinear interaction [49, 6]. These fields must satisfy conservation of energy and momentum to have a signal emitted in the phase matched direction. Of the 48 quantum pathways possible for the field permutations for a third order process, eight contribute to the FSRS signal. These are shown in Figure 5.3. Examining the pulse sequences for all of the FSRS pathways, it can be noted they are all different orderings of the fields A_L*, A_L, and A_S, the exact same fields

that are in the Stimulated Raman Polaziation described in Equation 3.22. This is no coincidence and all results applying to SRS from Section 3.2 can be applied to FSRS without alternation.

The first three paths in Figure 5.3, Resonant Raman Scattering I (RRS(I)), and Hot Luminesencence I and II (HL(I) and HL(II)), collectively produce the sharp, Stokes shifted peaks that are observed in SRS as well as FSRS. The width of these peaks will be determined by a combination of the vibrational lifetime along with the pump pulse. Their intensity will depend on the vibrational populations. This can be seen as all three pathways excite the bra side up with a pump pulse and the probe pulse knocks the bra back down. This mimics the stimulated emission process associated with SRS, as was seen in Equation 3.4. The ket side merely satisfies conservation of energy and momentum needed to observe a signal in the correct direction.

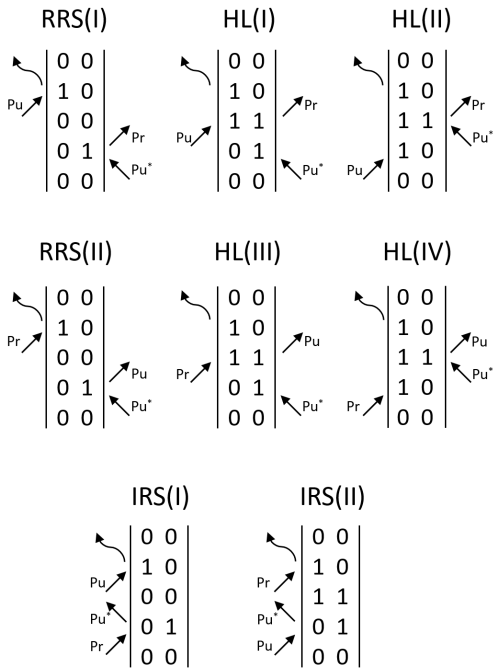

Figure 5.3: Feymann diagrams depicting the eight quantum pathways the are responsible for the FSRS signal. RRS stand for Resonant Raman Scattering, HL stands for Hot Luminescence, and IRS stands for Inverse Raman Scattering.

The Inverse Raman Scattering I (IRS(I)) pathways is responsible for the sharp Anti-Stokes polarization. Similarly to in the case of the SRS(I) pathways, the sharp spectral features are associated with a state being excited and driven down with a pump and probe pulse. However, in IRS(I), the probe pulse excites the electron up

and the pump actually drives it down. This fully captures the depletion aspect of the Anti-Stokes frequency response seen in Equation 3.4.

In the pathways labeled RRS(II), HL(III) and HL(IV) as well as IRS(II), the Stokes/probe fields are not interacting with the pump field, and the two pump fields are just exciting an electron up with one and then driving it back down to its initial state. As a result, no vibrational information is encoded within them. In the non-resonant case, the polarizations arising from the combination of RRS(I), HL(I) and HL(II) are equal magnitude and opposite sign to IRS(II) contributions, resulting a complete destructive interference of between the four pathways' emissions [11, 62, 6]. This in essence, means the probe passes through the sample without interacting. In the resonant case, where the pump excites electrons to the first real electronic state, the pump will cause some electronic transition and, as a result, the signal will experience spectral shifts and dispersive lineshapes [63, 64, 65, 66]. As the energy levels excited to between RRS(II), HL(III), HL(IV) and IRS(II) are no longer identical, they will not cancel each other out and lead to dispersive line-shapes and a resonant background [67].

FSRS has several advantages over other ultrafast vibrational methods that can provide similar information, like Coherent Anti-Stokes Raman Spectroscopy (CARS) and Coherent Stokes Raman Spectroscopy (CSRS). Because the FSRS signal arises from the SRS pathways, the process is innately phase matched [35]. As a result, the FSRS signal is emitted in the direction of the probe pulse. Accordingly, if the pump and probe beams are aligned in a noncolinear geometry, isolating the relatively weak probe spectrum/FSRS signal from the intense pump spectrum can accomplished geometrically. This strong signal directionality allows for background signals, such as florescence, to easily be easily avoided. Additionally, as the spectra are directly

comparable to those of SRS, signal interpretation is substantially easier than in CARS and CSRS.

5.2 FSRS and time-bandwidth products

An especially interesting aspect of FSRS arises when examining the time bandwidth products of FSRS experiments. Time-bandwidth products are a standard measure of the experimental implementation in ultrafast spectroscopy. They are found by multiplying an experiment's temporal resolution by its spectral resolution. As time and frequency are conjugate variables, there exists a lower limit on the accuracy to which both can be known simultaneously, as defined by the Heisenberg Uncertainty principle [6]. If an experiment utilizes transform limited pulses, the time bandwidth limit by the Heisenberg Uncertainty Principle is 5000 $cm^{-1}fs$. FSRS experiments have been known to achieve time bandwidth products of 500 $cm^{-1}fs$ [47].

This apparent breaking of the Heisenberg Uncertainty Principle has been extensively debated. It was mainly argued that although the product of the time duration of the femtosecond pulse and the spectral resolution of the FSRS spectra equals a number below the Heisenberg limit, the signal was, in fact, emitted over a time that corresponds to the conjugate time limit associated with the picosecond pump[5]. However, even the skeptics are now in agreement that FSRS spectra do not violate the uncertainty principle, although they do have time bandwidth products below the Heisenberg limit [47].

This surprising result arises from a pairing of pulses with quite different durations /bandwidths and the nonlinearities associated with SRS. In FSRS, each pulse individually obeys the uncertainty limit. As the electrons in FSRS are excited

to their virtual state by the picosecond pulse, their energy spread determines the spectral resolution. In turn, the temporal resolution of FSRS is determined by the duration of the femtosecond probe pulse. As a result, the time bandwidth product of FSRS can be far bellow the Heisenberg limit for a single pulse, allowing for simultaneous spectral and temporal resolution better than 100 fs and 10 cm^{-1} [47].

5.3 FSRS standard apparatus

In the literature, the standard experimental setup is centered around a 1 kHz, Ti:Sapphire Regenerative Amplifier, with 1W average power output [68]. This system provides the high intensity light needed to observe a strong FSRS response. The output of the amplifier is separated into three beams. A majority of the power is dedicated to the Raman pump pulse, as converting from a femtosecond to picosecond pulse is innately inefficient. The pump is usually produced by either spectrally filtering the fundamental of the Ti:Sapphire laser or using the fundamental to pump a NOPA, whose spectrum can then be then spectrally filtered to achieve a picosecond pulse. It is typical for the NOPA to provide a tunable actinic pump pulse, as the tunablity makes it ideal for tuning to a resonance to excite some effect within the sample. Alternative methods for obtaining the actinic pump are frequency doubling via SHG, or frequency tripling the Ti:Sapphire fundamental output [68]. The remaining energy is split to create a probe pulse, generally just a few milliwatts or microwatts of the fundamental. Once the Raman pump, Raman probe, and actinic pump pulses have been generated they are focused onto the sample in a colinear geometry. The pump pulse is chopped at an integer fraction of the the repetition rate in order to create an alternating sequence of FSRS signal spectra and probe spectra, which can then be subtracted in order to generate the

gain spectra. The light in both cases is dispersed by a spectrometer and detected by a photo-diode array(PDA) [68]. These are superior to CCD's in that their well capacity, the amount of charge each pixel can hold before saturating, is ten to one hundred times higher than a spectrometers CCD array. Additionally, a PDA can be linked to a lock-in amplifier to increase signal to noise ratios by integrating the signal with a sinusoid at the chopper frequency.

Chapter 6

FSRS as a probe of phonon dynamics

The goal in realizing condensed matter FSRS is to observe interactions between phonons in 2D materials on ultrafast time scales in order to correlate changes of temperature, phonon energy, and phonon populations. Substantial modeling and theoretical work has gone into such areas[30, 69, 31], but experimental data is largely lacking [21, 23]. As FSRS can provide this information on ultrafast time scales, it can further provide insight into non-equilibrium thermal populations.

Figure 6.1 depicts the different sample arrangements that would systematically provide insight into the true nature of confined non-equilibrium thermal transport. Of particular interest would be studying the variation in vibrational cooling times and couplings as the number of layers of the structures are varied, providing a baseline into the out of plane vibrational interactions between adjacent layers. Since Raman provides material dependent peaks, FSRS would separately measure the dynamics of the samples as well as the substrate. Heat transfer between the two would be readily identified in the FSRS spectra. These results could then be compared to the

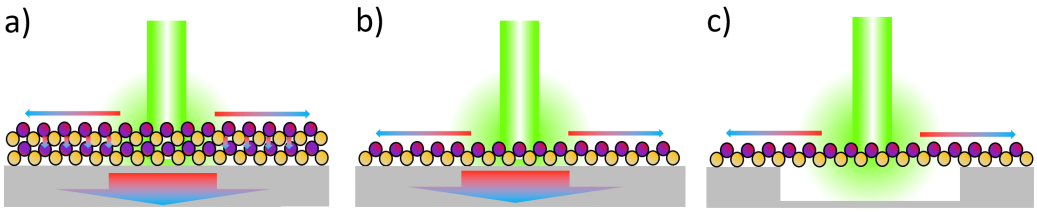

Figure 6.1: Rendition of how thermal transport might vary in a) a several layered structure on a bulk substrate, b) a 2D crystal on a bulk substrate, and c) suspended quantum confined material. Note in a) the additional arrows between adjacent layers.

data from a 2D crystal that had been suspended, allowing for the study of a strongly confined thermal transport.

The temperature of a sample can be resolved by measuring both Stokes and Anti-Stokes shifted light, so a coarse result of the FSRS experiment would be the tracking the rate of cooling of the 2D crystals in the various geometric arrangements of Figure 6.1. The suspended crystal would be expected to have the slowest thermal transport due to the fact that the heat can only move laterally. Adding a substrate and then more layers would expedite the cooling process [70], as the contact area has substantially increased.

A more interesting result would be resolving the individual vibrational modes interacting with one another and relate them to the temperature of the system. FSRS has the capability to resolve the hot optical phonon transport that has been theorized to occur in the first few hundred femtoseconds of cooling [71, 29]. As most 2D materials have rich optical phonon modes, as seen in Figure 4.5, observing the hot phonon dynamics and their relationship to a "temperature" could provide substantial insight into the quantum mechanics of non-equilibrium thermal transport.

A further goal, which FSRS data would only be a part of, is to cross-correlate phonon dynamics with electronic dynamics, opening possibilities for perhaps driving

or suppressing certain electronic interactions with vibrational modes. For instances, if a correlation was found between an exciton disassociation and the emergence or increase of a phonon mode, one could potentially drive the vibrational mode, using SRS or some other technique, to disassociate the exciton prematurely. Alternatively, one might be able to drive other modes and suppress the dissociating mode in order to increase the exciton lifetime. This is, admittedly, a far off goal, but offers exciting capabilities for carrier control.

Damage thresholds are the main obstacle in a condensed matter FSRS experiment. The number of atoms present in a focal volume of mono- to few- layer crystals is substantially smaller than the number in the liquid samples traditionally used in FSRS. This means that the repetition rate and laser fluence on the sample must be finely balanced.

6.1 FSRS iteration 1

The first iteration of the FSRS apparatus is shown in Figure 6.2. The basis for the experiment is a Spectra Physics Spirit 1040-8 Regenerative amplifier laser that has 8 W of output at 1040 nm, operating at 200 kHz. Half of the output pumps a Spectra Physics NOPA 3H, and the other half pumping a pair of nonlinear crystals to generate second and third harmonics. The NOPA 3H system was purchased from Spectra alongside the Spirit and produces between 1 to .05 μJ of 30 to 70 fs pulses of tunable wavelength centered between 500 and 950 nm. The tunablity of this system makes it an ideal option for producing Raman probe pulses that can be set to a specific vibrational energy. The other half of the Spirit output was used to pump a SHG crystal to produce approximately 10 μJ of 520 nm light. This light is then spectrally filtered to a bandwidth of a few nanometers to produce the picosecond

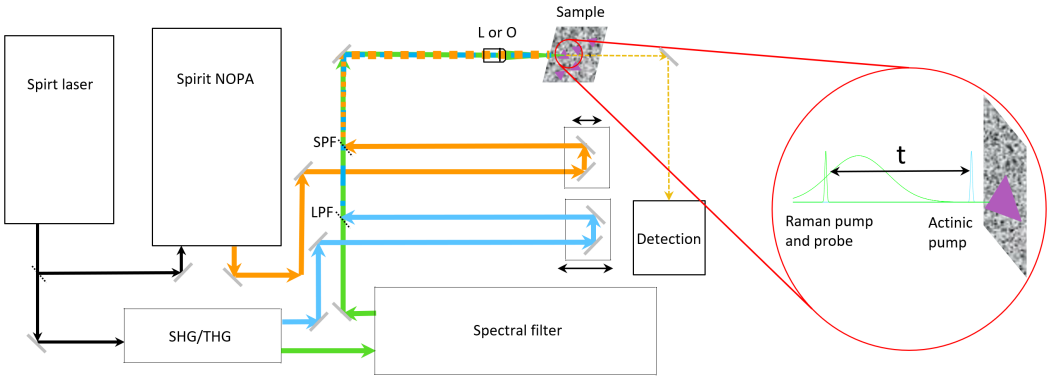

Figure 6.2: Diagram of the Siemens lab's first FSRS experiment. The black line represent the fundamental output of the Spirit. The green lines are the second harmonic path and the blue is the the third harmonic. The orange represents the output from the NOPA. The yellow dashed lines are the signal. To the right, the FSRS process is depicted. The third harmonic flash heats the sample that the FSRS pulses then probes the thermal transport. L is lens, O is objective, SPF is short pass filter, LPF is long pass filter.

Raman pump beam. Some of the unfiltered 520 nm light is additionally recombined with the fundamental 1040 nm output via SFG to produce a 347 nm actinic pump. UV light is strongly absorbed by most solid state materials, producing a flash heating of the system.

The Raman probe and the actinic pump are both connected to electronic delay stages in order to control the time delay between all three pulses. The conlinear setup combined the different beams using a series of long pass filters to combine the different wavelengths of light. These are then focused onto the sample using a 20x microscopy objective. In both cases the signal beam is collected and sent to an electronically cooled spectrometer for detection.

Harmonic Generation

To provide the Raman pump as well as the actinic pump, Second Harmonic Generation (SHG) and Third Harmonic Generation (THG) are performed. Type I SHG is performed in a 7 mm Lithium Triborate (LBO) crystal. The emitted green and fundamental light are then passed through a calcite delay plate to realign the two orthogonally polarized pulses in time. These pulses then pass through an additional LBO crystal that had been cut to optimize phase matching between the 1040 nm fundamental pulse with polarization parallel to the ordinary axis and the 520 nm pulse polarized parallel to the extraordinary axis. The result of the Type II SFG is a 347 nm pulse with horizontal polarization. This setup is designed to generate a small amount of 347 nm light while optimizing the output at 520 nm. With a 4 W pump, it is typical to produce 1.6 W of 520 nm light and 150 mW of 347 nm light.

After generation, the three beams are separated from one another using dielectric filters. The 1040 nm light was sent to a beam block and is not used further in the experiment. The 347 nm light is sent to a delay stage and focusing optics without alteration. The 520 nm light is expanded to a 4 mm width with a telescope and then spectrally filtered to create the Raman pump pulse. Spectral filtering is achieved using a 1,800 g/mm grating. The dispersed light is collimated by a 1 m focal length lens. After an additional meter of propagation, a section of the spectrally dispersed beam is blocked by a pair of matte black razors placed in front of a mirror. That mirror back reflected the beam displaced vertically. After passing back through the lens, the beam is recombined by the grating and sent to a delay stage and then to the sample.

NOPA

A Spectra-Physics NOPA 3H is a foundational aspect in the initial implementation of the FSRS project. This device has several design aspects that are worth mentioning. A NOPA requires a high photon energy and intensity pump to amplify a weak, white light seed. This particular system utilizes the 347 nm third harmonic of the Spirit output as a pump. The generation of third harmonic can be accomplished either by a third order parametric addition of three photons of the fundamental beam, or a by a SHG process followed by a SFG of the second harmonic and the fundamental beam to create a photon at the third harmonic. The latter process tends to be much more efficient than the first process. To optimally generate the third harmonic, the initially vertically polarized pump beam passes through a half-wave plate to rotate the polarization to have both vertical and horizontal components. The beam is then sent through a birefringent crystal, delaying the horizontally polarized portion of the pump from the vertical component. In essence, this creates two pulses offset by a few hundred femtoseconds, one vertically polarized and the other horizontally. These pulses then pass through a SHG crystal, which takes two photons from the vertical polarization and emits second harmonic at a horizontal position. The horizontally polarized fundamental pulse is not frequency doubled as it is polarized orthogonally to the non-centrosymmetric axis of the crystal. Now, due to the differences in the refractive index between the green second harmonic and the fundamental, the green second harmonic is delayed and is now overlapped with the horizontally polarized fundametnal. These are then combined Type 0 SFG to generate the third harmonic. Balancing the intensities of the horizontally second harmonic and fundamental beams can be achieved by rotating the half wave plate. This can be used to optimize the conversion efficiency, which can optimally reach about 30%.

The system also features a two-stage amplifier. The pump and probe pass through nonlinear crystals twice in order to fully optimize the pump power that was generated. The second stage usually adds more than an order of magnitude of power when compared to just the first stage.

Additionally, the system has an integrated compressor to minimize pulse duration. The system is set up so that after passing through both prisms, the beam hits a rooftop reflector and passes back through the same prisms, vertically offset, where it then exits the box as a 20 to 70 fs pulse depending on the wavelength of the output.

The entire system features computer controlled delays between all of the beams as well as computer controlled positions for the DFG crystals as well as the pulse compressor. As the white light source is chirped out, small alterations of the delay stages are needed to optimize the output power of a given color. Additionally, the DFG crystals need to be rotated in order to achieve ideal phase matching conditions. These slightly different values are collected at every 10 nm within the tuning range and used to generate a set of parameters curves that were used to create smooth tuning of high powered and well compressed pulses at any wavelength desire in between the points. Resetting or realignment of any portion of the NOPA results in the need for new tuning curves.

From the output of the NOPA, between 5-15 mW of power at the selected wavelength are used as the Raman Probe pulse. After passing a delay stage, this light was combined using a reflective optic nearest to the focusing optics in order to mitigate pulse stretching by passing through any optics to give the FSRS experiment optimal temporal resolution.

Sample and detection

There have been no reports of FSRS use on 2D solid state systems, so the intensity of light that would be needed to observe the FSRS response was estimated. For comparison, the reported pump pulse energy from successful FSRS experiments on chemical systems is on the order of several to tens of μJ focused down to 50 μm spot size. For the apparatus, a nominal pump pulse of similar duration would be on the scale of .1 to 1 μJ. Raman cross sections for solid state materials are approximately two to three orders of magnitude larger than those seen in liquid phase[35]. However, the number of scatterers used in a liquid phase experiment can be substantially larger than those in the condensed phase by a similar two to three orders of magnitude. Based on these values, the focal spot size to achieve a comparable signal was estimated to be between 50 μm and .5 μm.

To span this range in focusing needs, two separate focusing pathways are available for the FSRS experiment. Both arrangements use a colinear geometry for the Raman Pump and Raman probe pulse and they can be altered between using a flip mirror mount. For the larger spot size, the 3 mm beam is focused with a 4" focal length, fused silica lens that is anti-reflection coated between 350 nm and 1100 nm to achieve a spot size of approximately 44 μm. To achieve smaller spot sizes, a microscope mount is used in combination with either an infinity corrected a 4x .17 NA objective with spot size of approximately 4 μm or an infinity corrected 5x .7 NA objective with a spot size of approximately .5μm.

For detection, a Horiba iHR550 spectrometer is used with a Horiba Synapse CCD. The Horiba spectrometer has a 550 mm focal length and contains 150 g/mm, 900 g/mm, and 1800 g/mm, resulting in a spectral resolutions between .2 nm and .02 nm. The system connects to a computer utilizing a USB cable and the gratings

and wavelength position can be controlled through a LabView interface. Coupling into the spectrometer is achieved by matching the beam's numerical aperture to the aperture of the spectrometer. The Synapse CCD is thermo-electrically cooled to reduce background noise. The quantum efficiency of the model in the visible range from 40-50%. Acquisition time, number of spectral acquisitions, and gain can all be controlled with a LabView program.

Data analysis

The spectrometer data is output as a .txt file. The LabView program was altered so that each spectrum acquired during multiple-acquisition data collection is in an adjacent column with the first column in the array representing the pixel. The pixel to wavelength conversion is accomplished in one of two methods. A coarse calibration curve based on the wavelength position read by the spectrometer for the grating works sufficiently well for the 150 g/mm and 900 g/mm gratings. For higher resolution, calibration was achieved using the 532nm laser line and the 520 cm^{-1} silicon Raman peak.

A MatLab code was created in order to subtract cosmic rays and other hot pixels during acquisition. The program examines spectra taken sequentially in time and compared pixel intensities from one spectra to the next. If there is an increase from one acquisition to the next that was more than an order of magnitude increase, that pixel is revalued at the average of that pixels intensity from the previous spectrum with that from the following spectrum. After hot pixels and cosmic rays have been subtracted, the spectra are added together and averaged to increase signal to noise ratios.

Challenges and lessons of first iteration

Although the NOPA system was a commercial product, it experienced substantial difficulties in its operation. The harmonic separator, which reflects the 347 nm pump from the 520 nm and 1040 nm pump experienced degradation after approximately 20 hours of operation. Initially, it was assumed that this was due to either the high peak and average output of the third harmonic or perhaps debris from the air collecting on the optic, resulting in a cascade burning on the dielectric filter. A replacement was ordered and installed by a Spectra-Physics technician who also instructed me on the replacement procedure. The replacement was burnt within 10 hours of use. By shimming the mount with a washer, an additional 10 hours of use could be achieved, but the retuning of the system required a majority of that time, making it an impractical solution.

It was then discovered that there was a manufacturing issue with the harmonic separator and they were even degrading in a nitrogen rich environment independently of any laser fluence. A new batch was prepared and mailed to us component, I performed the installation. This version did not degrade, but then other optics further down the beam line began to degrade throughout the system, including the DFG crystal as well as several of the focusing lenses. After close to 13 months of part swapping and continued damage, the NOPA was returned and work on the second iteration of the FSRS setup began.

Part of the way through the experiment we discovered that a back scatter geometry does not work for SRS or FSRS, although it will work for SpRS. This led to complications with the mechanically exfoliated samples, as the silicon substrates the 2D materials were exfoliated onto are non-transmissive at the frequencies used in the experiment. Transfer of the exfoliated samples can be done, but it is

exceptionally challenging and if transfered onto a transmissive substrate locating them is nontrivial. This led to the purchasing of several full coverage graphene samples mounted on quartz as well as a ReS_2 sample on sapphire.

Detection also posed several problems. To measure the gain, a pump on/ pump off collection sequence is needed. To optimally implement this, the frequency chopping would be synced to the shutter on the spectrometer for collection. Another issue that arose was saturation of the spectrometer CCD. The well depth on these systems is quite low compared to the dual array photodiodes used in low rep rate FSRS experiments. As a result, even a few milliwatts of power passing through the sample led to substantial saturation.

In the FSRS setup, none of the pulses are of identical wavelength or duration, making the alignment of the pulses temporally quite challenging. Fortunately, the basis of a cross correlation is to utilize a nonlinear signal to align the beams. As SRS is a nonlinear signal, we decided to search for the FSRS signal as an alignment procedure for the pump and probe pulse. This has been reported in the literature to work quite well. However, we did not observe any FSRS gain as a majority of the time was spent repairing the NOPA system.

6.2 FSRS iteration 2

The second iteration of the FSRS setup is more simplistic and focused on directing as much power as possible into the Raman pump beam. 7.2 W of power is directed into the SHG and then spectrally filtered to produce a Raman pump pulse that is roughly twice the intensity of the pump in the previous iteration. The remaining 10% of the fundamental pumps a YAG crystal to produce a continuum spectrum. In this case, no actinic pump was created as the primary goal is to just observe a FSRS

signal. These beams are focused in a non-colinear geometry and were detected by the same Horiba spectrometer.

Harmonic Generation

For the second iteration, the main output of the laser is split with a half wave plate and a thin film polarizer. 7.2 W of power was directed through a 7 mm LBO crystal, resulting in 3.5 W of output at 520 nm. This is then spectrally filtered in an identical fashion to the previous attempt. This setup yields almost twice as much power in the Raman pump pulse.

WLG

Without a NOPA, the Raman probe pulse is created using Super Continuum Generation (SCG) in a Yttrium Aluminum Garnet (YAG) crystal. The beam is focused with a two inch focal length lens and collected with a 1" focal length lens mounted to a two-axis translational stage. The YAG crystal is mounted on a translation stage to move it in and out of the focus of the beam. The continuum is optimized by rotating the half wave plate to adjust the fluence contributing to the pumping and by adjusting the position of the YAG. Even though power is slightly lower, it is ideal to have the continuum's filament begin near the end of the crystal in the beams propagation direction. Focusing in the center will yield higher powers but can often have numerous continua which can all be temporally distinct, resulting in a continua pulse train [37]. The optimal power output achieved for a stable continuum is .6 mW using an 800 mW pump.

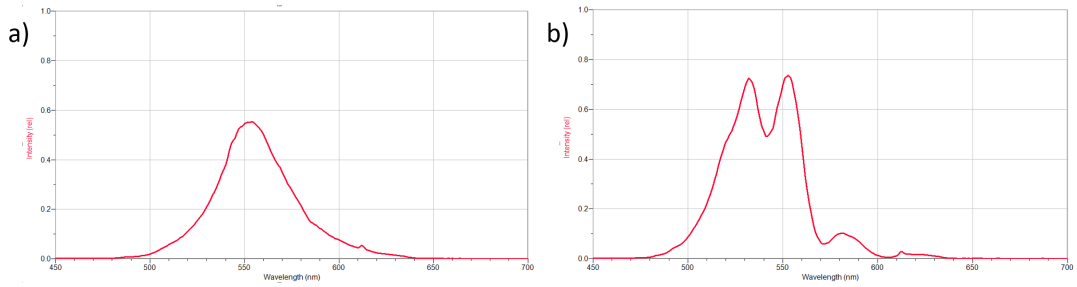

Figure 6.3: Comparison between a) a single filament continuum spectrum generated at end of the YAG plate and b) a multiple continuum filament from the center of a YAG crystal. The additional peak seen in b) is the result of a second continuum filament being formed.

Sample and detection

For the second iteration a new setup of focusing and imaging optics was setup. In this attempt, each beam is focused individually onto the sample. By mounting the lenses on translation stages, the effective spot size can be readily adjusted to optimize overlap between the pulses. A 150 mm plano-convex lens that was AR coated for the visible is used to focus the Raman pump pulse and a 100 mm, 350 nm to 1100 nm AR coated lens is used for the Raman probe pulse. The samples are mounted with double sided tape onto a translational stage. As objectives and micro-crystals had been replaced by a lenses and a 1 cm square chemically grown graphene sample, the lateral adjustment has been abandoned.

For detection, two methods are used. The first is the spectrometer used in an identical fashion as before. The alternative utilizes a side exit of the spectrometer with an adjustable slit to convert the spectrometer into a monochromator. The Horiba iHR550 can swap between modes with the LabView program. The center pixel of the CCD array corresponds to the center of the slit in monochromator mode.

The Raman pump pulse is used to collect a SpRS signal from the sample for alignment to a specific peak. The grating position is then altered so that the peak

was positioned at the center of the CCD array, and accordingly the center of the monochromator slit. The light that passed through the slit is then connected to a photodiode that is coupled to a Stanford Research SR830 Lock-In Amplifier.

Lock-In amplifiers present a substantial benefit in signal to noise ratios over a spectrometer. By integrating the signal that it receives from an outside source with a sinusoidal function modulated at the frequency of the expected signal, noise from stray light, electronics, or other sources that is emitted at frequencies distinct from the signal are attenuated. The sharpness of the filtering will increase signal to noise ratios, but at the cost of longer integration times. This amplifier is set to look for signal at the frequency corresponding to the beat between the rep rate of the laser system and a mechanical chopper. A FSRS response from the sample would manifest itself as a gain in this signal. The main drawback to this method is that the entire spectrum cannot be measured simultaneously. To get around this, the lock-in is used to find the time at which the pulses are temporally overlapped. The delay stages is fixed at this position and the detection would then be swapped to the spectrometer to see the full spectral response.

Challenges of 2nd iteration

One drawback of the 2nd iteration was the pulse duration of the Raman probe pulse. It was generated with SCG, whose spectrum are usually emitted over a time scale on the order of the excitation pulse [37]. In the case of an 50 fs probe pulse, this doesn't present a major problem. But as the pump is 400 fs, the continuum probe pulse likely had a fairly long duration. The problem in the setup is exacerbated as the focusing and collimation optics used were short focal length lenses. These thick lenses stretched out the pulses further. Additionally, as the SCG is the result of self focusing, the beam takes up a large portion of the NA of the spherical lens. This

introduces a substantial amount of spherical aberration that is then combined with the chromatic aberration that arises from trying to collect light that spans close to 100 nm of the visible light spectrum with a single lens. A superior setup would be a pair of .5" off axis parabolic mirrors (OAP) for focusing and collimation. OAP do not suffer from the chromatic or spherical aberration that is found in lenses or spherical mirrors. Additionally, they would not increase the pulse duration.

It would be further beneficial to have compressed the pulse prior to use in the experiment. Compression prisms that are optimized for use in the visible are challenging to find commercially. A grating setup would be possible, but the losses associated with them can be quite high, especially for the weak .6 mW probe. The ideal option would be to use chirped dielectric mirrors, as the compression can be achieved with very low losses, which is ideal for this case where the powers are already low.

6.3 Ideal Setup

As the FSRS experiment was started from a blank slate, an immense amount of time was dedicated to designing what the idea system would be. Having now tried two iterations of the experiment in practice, an ideal setup now has a more concrete vision. The system's probe pulse would be exceptionally broadband in order to capture stimulated emission from as many vibrational modes as possible and optimize the temporal resolution of the experiment. Additionally, the pulses would be tunable through the visible spectrum. The actinic pump would share all of the above traits as the probe pulse, with the addition that it should be able to extend into the UV. The Raman pump pulse would be high intensity and spectrally narrow. It would be tunable through a range similar to the probe pulse. Further,

the ideal FSRS experiment would, on top of these traits, be capable of achieving sub diffraction limit resolution through some variation of the STED process. Accordingly, the system would boast a tunable STED beam [72]. For more information on STED, see Chapter 7. As super resolution SRS has been shown capable with both an additional picosecond pulse [73] as well as an additional femtosecond pulse [33], the STED pulse could vary depending on the exact nature of the setup.

6.3.1 OPA design

As part of envisioning this ideal apparatus, several OPA variations were thought of.

Dual NOPA

After working with the commercial NOPA, it was realized that a few mW of power were sufficient for the probe and that a multi-stage amplifier was unnecessary. A system with two independently tunable pulses would be far more preferable. A schematic for a Dual NOPA is shown in Figure 6.4. In this particular design, the fact that the the second harmonic must be generated in order to create the third harmonic is taken advantage of. The SHG and THG ratio can be altered by rotating the half wave plate or the delay plate the start of the system, akin to the manner it was produced in the commercial NOPA system.

After separating the harmonics, the remaining fundamental is focused into a YAG plate for WLG. The continuum produced from this is then split into two arms, each with its own controllable delay. The white light and harmonics are focused into a OPG crystal where the white light is amplified. The wavelength is tunable by rotating the OPG crystals and altering the time delay between the pulses.

Alternatively, one could generate either the second or third harmonic optimally and then split that beam into two separate beams. Ideally, this would be done with a half wave-plate and thin film polarizer so that the pump power to each arm could be adjusted, varying the intensity of the amplified light in each arm.

Simple OPA

In the instance where high intensity tunable light is needed, a multi-stage amplifier is required to convert as much of the pump energy as possible. A simple, multistage, OPA system that does not require separation and recombination of pump and signal beams was designed, shown a in Figure 6.4b). The second harmonic is generated via Type 1 SHG process, so that the pump and fundamental are polarized orthogonally. The harmonic is filtered from the fundamental and sent to a delay stage. The remaining fundamental is focused into a white light crystal. The two beams are combined into a colinear geometry with a long pass filter. Next, both beams propagate through an OPG crystal. These crystals should be long to optimize the OPG. However, as a result of differences in the index of refraction between the pump and amplified continuum section, the amplification will stop as the pulses temporally walk off from one another.

It is typical to then separate the beams with a filter, adjust the time with a delay stage, and recombine them for further amplification. In this design, the pulse are temporally realigned with a birefringent crystal. The time adjustment can be tuned by rotating the crystal or, in extreme cases, by using a thicker crystal. The two beams then pass through an additional OPG crystal, where the gain is further amplified. In theory, this process could be repeated until the pump and signal are of equal intensity.

Fourier OPA

A relatively recent innovation is known as a Fourier OPA or FOPA [74]. So far, these systems have only been implemented in the IR wavelengths. However, a schematic for a visible FOPA can be seen in Figure 6.4c). The harmonic pulse is generated in a method identically as in the Dual NOPA and Simple OPA. It is then expanded laterally with a cylindrical mirror and directed slightly upward. The harmonic is then collimated laterally with a spherical mirror, that focuses the beam back down to the the initial vertical plane. At this point, a set of OPG crystals are placed.

WLG occurs in a YAG plate and is collimated and the fundamental is filtered out. The continuum is incident on a grating, dispersing the colors laterally. This light is then collimated laterally with spherical mirror and then focused at the same position as the harmonic.

As the continuum colors are spatially offset, each OPG crystal can be adjusted to optimize the amplification of the portion of white light overlapped with it. As a result, the entire continuum can be amplified simultaneously, resulting a several hundred nanometer bandwidth of amplified light. This light propagates colinearly and is collected by a spherical mirror and sent onto another grating for recombination. The residual pump, in this design, is sent to a beam block. The resulting beam should be emitted in a mostly compressed form, but the position of the second grating can be adjusted to compress the light further if needed.

6.3.2 FSRS ideal setup

The ideal design centers around a 200 μJ regenerative amplified laser system operating at 500 kHz. The apparatus is shown in Figure 6.5. Approximately 10%

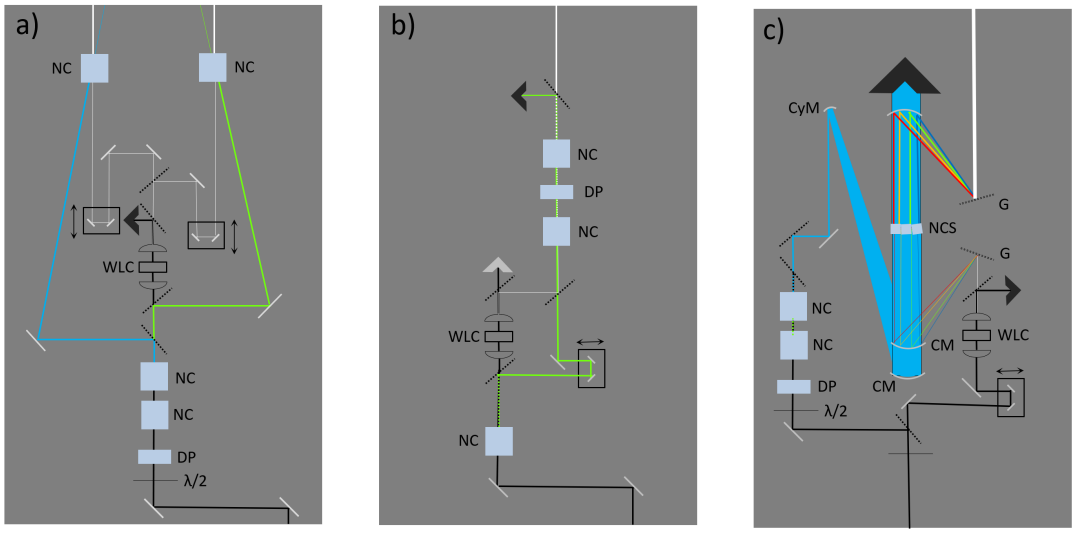

Figure 6.4: Schematic diagrams for several OPA variations for the FSRS experiment. The Dual NOPA in a) has two independently tunable NOPA setups. Part b) shows a schematic for a simple, two step OPA. c) shows a diagram for a Fourier Optical Parametric Amplifier.

of the system would go to pump a NOPA or FOPA system, highlighted in green in Figure 6.5. 10% of the output from the NOPA/FOPA will be used as a seed pulse for the picosecond OPA (PS-OPA) that will be discussed later. The remaining 90% of the NOPA /FOPA beam would be frequency doubled, occuring the red highlighted area in Figure 6.5. Its fundamental would be separated from the second harmonic. The second harmonic would be used as the actinic pump pulse and the original FOPA/NOPA beam would form the Raman Probe pulse.

The remaining 90% of the fundamental power would pump a Second Harmonic Bandwidth Converter (SHBC), highlighted in blue in Figure 6.5. In this apparatus, the input beam would be split into two beam which would then receive positive and negative chirp. Traditional methods for chirping rely on the use of grating to spectrally disperse the bandwidth of the pump pulse. This diverging light is then collimated with a lens. To recombine the pulse without chirp, a mirror is placed

exactly one focal length away from the collimating lens and the beam is reflected back through the lens and to the grating. By altering the position of the mirror, one can produce positively and negatively chirped pulses. This method is cost effective, as the optical components involved are fairly inexpensive. However, gratings are innately inefficient, so the losses just from the gratings in this type of SHBC's can be optimally 40% or so. A far more efficient alternative is to use chirped mirrors. These mirrors can chirp a beam while losing ¡ 1% of power and can be designed to have both positive and negative chirp.

After being stretched by dielectric mirrors, the beams would then be combined non-colinearly in a SHG crystal. The strong positive and negative chirping in the two pulses means that the the red portion of one spectrum is added to the blue spectrum of the other, resulting in a sum frequency of twice the center wavelength of the pump spectrum for all wavelengths inside the spectrum. The net result is a spectral compression of the pump beam by more than an order of magnitude with a respectively small lose of the scale of 50%, roughly the quantum efficiency of the SFG processes. Additionally, as a result of the phase matching in the noncolinear geometry, the narrow band second harmonic will be innately spatially filtered from the pump pulses that generated it.

The narrowband second harmonic would then be split in half and used a pump a pair of PS-OPAs that will be individually tunable and based upon the Simple OPA design. The white light seed for these will provided by the pick-off of the NOPA/FOPA system that has been dispersed by passing through glass. In each PS-OPA, the polarization of the pump and white light seed would be offset by 90 degrees and passed through a long OPG crystal. As a result of the difference in the index of refraction between the white light and the pump, the pulses would exit the OPG crystal temporally offset, preventing further amplification. This offset

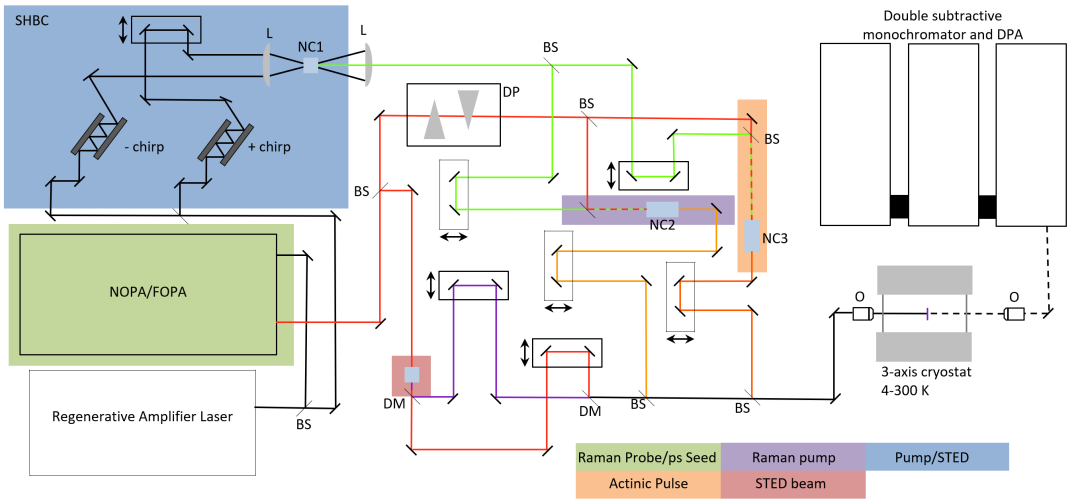

Figure 6.5: Schematic depicting the ideal FSRS experiment. Different colored lines are used to distinguish beams. BS = Beam Splitter, DM = dichroic filter, NC = nonlinear crystal, DP = dispersion prisms, L = lens, arrows = delay stages. The shaded backgrounds designate where each pulse for the FSRS experiment is generated.

would be compensated for by using a birefringent crystal, where the orthogonal polarizations can be used to delay the pulses independently by choice of crystal thickness. Once temporally realigned, the pump and seed would again pass through an OPG crystal. One PS-OPA would produce Raman pump pulse of appreciable power, tunable between 600 and 900 nm. The other beam would pass through a Spiral Phase Plate (SPP) in order to create a vortex beam with a singularity at its center. This beam will be utilized to induce a STED-like process to achieve sub-diffraction limit FSRS signal from the beam singularity.

All four beams would be recombined in a collinear geometry with the use of high or low pass filters and beam splitters. These would then be focused with either a microscope objective or an off-axis parabolic mirror onto the the sample. The sample would be mounted on a 3-axis motorized stage within a cryostat equipped for transmission spectroscopy. This would allow for suppression of all room temperature

vibrational modes and restrict thermal activity as a result of the actinic pump. The emitted signal would be collected by an objective or OAP and sent to a double subtractive spectrometer. As Raman filters are expensive, a double subtractive spectrometer would allow us to remove the Raman pump as well as the STED beam from the phonon spectrum at whatever wavelength is chosen. Ideally, the detection at the end of the subtraction phase would be a photodiode array, such that lock-in detection could be utilized at all wavelengths simultaneously, increasing signal to noise.

6.4 FSRS Conclusions

The second iteration of the FSRS apparatus on solid state materials has been constructed. As of now, a FSRS signal still has not been observed. However, the lessons of the last two years give insight into the future possibilities and directions for this experiment. Promising results are still expected once the system is functioning.

From a technical standpoint, finely balancing damage thresholds and signal is still a concern, although work on Surfaced Enhanced FSRS [13, 75], supports that this will be surmountable. Another technical improvement would be more efficient detection. A CCD with a large well capacity or a photo-diode array that supports full spectrum lock-in detection would be optimally suited for the experiment.

Another challenge to be faced in FSRS is to resolve low energy vibrations in the systems. For 2D materials like MoS_2 and ReS_2 most modes are under 500 cm^{-1}, which is low for a FSRS signal, although vibrational modes as low as 80 cm^{-1} have been taken with FSRS [62]. This presents a further challenge for observing breathing modes in 2D materials, which are often less than $50cm^{-1}$ [19, 28]. These would be extremely challenging to resolve as it would require a very spectrally narrow pump and

abrupt filter, which would then need to have an even higher intensity to experience stimulated emission gain.

The main drawback of the FSRS discovered over the last two years is its inability to be performed in the backscattered direction. This limits implementation to optically transparent samples. For the case of 2D materials, this is not problematic as they are transparent in their mono- to few- layer form. However, it does limit FSRS ability to study bulk solid state materials that might not be stable in few-nanometer thick layers.

Despite these drawbacks, however, the additional pump power of the second iteration of the FSRS experiment is capable of achieving several micro-joule pump pulses, placing it in the same category as the traditional molecular FSRS system pump powers, leaving pulse alignment as the final, relatively simple obstacle to be overcome. A new graduate student next year will be taking over the project and using the second iteration of the experiment to perform solid state FSRS. This will be a publishable result that is based primarily on the work described in this thesis and will be notable addition to the FSRS literature.

Chapter 7

Nonlinear optics and the Uncertainty Principle

As part of the investigation of the capabilities of nonlinear optics, it will become relevant to have a grasp of the nature of the Heisenberg Uncertainty Principle.

7.1 The Uncertainty Principle

In the quantum mechanical picture, the Heisenberg Uncertainty Principle limits the simultaneous observation of non-commuting operators. For any two operators, A and B, this limit is mathematically defined by

$$(\Delta A)(\Delta B) = i\hbar[A, B], \tag{7.1}$$

where ΔA and ΔB are the standard deviations in the measured values of A and B and $[A, B]$ [45] represents the commutation of the variables. This gives the relations familiar from quantum mechanics class [45]:

$$[p_i, x_j] = \frac{\hbar}{2}\delta_{ij}, \tag{7.2}$$

$$[p_i, p_j] = 0, \tag{7.3}$$

$$[x_i, x_j] = 0. \tag{7.4}$$

This framework is limited to explaining systems which have quantum mechanical operators.

However, the Heisenberg Uncertainty Principle's true roots lie in wave mechanics, of which quantum mechanics is only a single example.

The classical nature of the Heisenberg Uncertainty Principle can be easily illustrated conveniently by discussing light. If there is a single frequency of light propagating everywhere, it will be impossible to describe the position of the wave, as it is uniformly spread over all space, as seen in Figure 7.1 a). However, the frequency of that wave can be precisely known. In the opposite extreme is a laser pulse, shown in Figure 7.1 b), where the pulse will have a definite position. In this instance, there will be an ambiguity about the frequencies contained in the pulse. So, from this classical example, it is shown that uncertainty is more accurately described as a wave phenomenon.

It turns out, any system for which a Fourier transform can be made between the variables will have an uncertainty relation between the two variable[45]. Immediately, this gives us another uncertainty relation,

$$[E_i, t_j] = \frac{\hbar}{2}\delta_{ij}, \tag{7.5}$$

or perhaps more familiarly,

$$[\omega_i, t_j] = \frac{1}{2}\delta_{ij}. \tag{7.6}$$

7.2 Bypassing the Heisenberg limit

A seemingly undiscussed power of nonlinear optics is its ability to bypass Heisenberg limitations. This capability is elucidated when examined from the context of quantum pathways driven in nonlinear interactions and the spatial arrangements of fields.

A very simple approach to discussing this can be found by remember the commutation relations between energy and time as well as position and momentum in Equations 7.2 - 7.6. From these simple equations, it is observed that the position of one wave, x_i, commutes with that of another wave x_j, as seen in Equation 7.4. If this were not the case, then the measurement of one beam's profile would increase the size of another separate beam's profile.

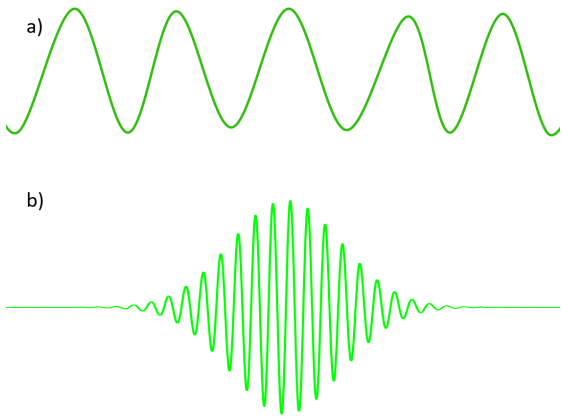

Figure 7.1: a) Single frequency field in comparison to a b) laser pulse.

Additionally, from Equation 7.6, if one laser's spectrum is measured with high precision, another's would then be broadened. Neither of these are physical. However, each beam independently satisfies Equations 7.2 - 7.6; focal spots are still limited by wavelength and pulse duration and spectrum still have their fundamental trade offs.

The commutation between spot sizes, band widths, and pulse durations of different beams allows for a physical mechanism for bypassing Heisenberg limits.

7.2.1 Spatial distribution of a single field

The most simplistic way for a nonlinear system to bypass the uncertainty relations requires a signal of at least second order with a field and a single field with a non-uniform spatial distribution.

This idea is clarified best with an example comparing the spatial resolution of a first order optical process excited by a Gaussian beam to the spatial resolution of a second order process excited by a Gaussian beam. Both beam profiles for the first and second order process are identical. The linear signal's spatial response will perfectly reflect the Gaussian profile of the excitation beam. As the polarization of a second order process is dependent on the square of the intensity, the spatial resolution of the second order processes' signal will be emitted as the Gaussian squared. This will result in a $\sqrt{2}$ increase in the spatial resolution for the nonlinear signal over the linear signal. Supposing now that each field independently is operating at the diffraction limit, then the nonlinear interaction has a spatial resolution that has surpassed the Heisenberg uncertainty relation for each individual field. But there is no contradiction here. Each beam independently is constrained by the Heisenberg uncertainty relation. However, the processes' dependence on the square of the intensity results in a steeper gradient of the signal near the center of the beam as opposed to its edges. Theoretically, this provides a method to increase spatial resolution nearly infinitely by just choosing processes in which higher and higher nonlinear processes are occurring. The limitations of this will play out according to

damage thresholds in the sample as higher order nonlinear processes often require higher and higher intensity fields.

7.2.2 Spatial overlap of fields

While the above situation can increase resolution by a fact of $\sqrt{n}$, there is a better way to achieve sub Heisenberg resolution in an experiment with lower order processes. As discussed in Section 2.1.2 nonlinearities can be thought of as driving an electron down various quantum pathways. The addition of another field at some point during this process can disrupt that quantum pathway and send electrons other directions.

It is the precise manipulation of this additional field spatially that allows for super-resolution measurements. As just discussed, the are no restrictions on knowing the positions of two separate fields. Suppose a set of fields, A, that will drive the quantum path, α. An additional field, B, when added to A, will suppress α and drive another pathway, β. Assume the signals from α and β are discriminable. If B is completely overlapped with the initial fields, A, all that will occur is a uniform driving of β. However, if the spatial overlaps between A and B are not uniform, the only place where the signal from β can be emitted is the area where B exists. So, if B is only present in a small space, the signal can only arise from that area.

A similar effect will arise if B covers all but a small portion of A. If the presence of B suppresses α effectively, the only signal contributions from α will be emitted from from small area where A and B are not overlapped. In both cases, A and B must obey the uncertainty relations expressed in Equations 7.2 - 7.6, but the resulting nonlinear signal, has no such limitation.

Perhaps the most famous method for Heisenberg breaking is the 2012 Nobel Prize winning method of STimulated Emission Depletion (STED) [72] microscopy. STED

microscopy utilizes one Gaussian beam and one Lagguere Gaussian (LG) beam, which can be described as an Gaussian profile with a zero intensity singularity at the center of the beam. The two beams are colinearly focused onto a sample. Where the two beams are overlapped, electronic depletion occurs, resulting in florescence suppression. However, as a result of the intensity singularity at the center of the LG beam, the only contributing field is from the Gaussian beam. In this very small area of the singularity, fluorescence will be permitted. As a result, the spatial resolution of the fluorescence can be enhanced by more than a factor of 10 [72]! As before, the uncertainty principle remains perfectly preserved for each individual beam.

Still other versions of exploiting nonlinearity for Heisenberg breaking exist. As discussed earlier in this thesis, Femtosecond Stimulated Raman Spectroscopy (FSRS) has provided ultrafast spectroscopy measurements with time bandwidth products of $.5ps * cm^{-1}$ [63], which is 30 times the Heisenberg limit of $15ps * cm^{-1}$. As the stimulated emission can only happen in the presence of both fields, the temporal resolution is determined by the femtosecond pulse. As a result of the mixing of the picosecond excitation and the femtosecond stimulated emission, the time-bandwidth product of the method is far below what is permitted by Heisenberg for a single field.

While the power of nonlinear Heisenberg breaking is exceptional, it does have several limitations that must be considered. One key aspect is the relative efficiencies of the processes being driven. If the additional field does not effectively drive the electrons down a different quantum pathway, then its impact is minimal. However, if the other alternative path has a high efficiency, then the uncertainty principle can be bypassed.

In some instances, this efficiency can be enough for Heisenberg breaking. In a FSRS experiment, the SpRS is occurring throughout the entire duration of the pump pulse, but the Stimulated emission signal has a factor of 10^6 to 10^8 enhancement over

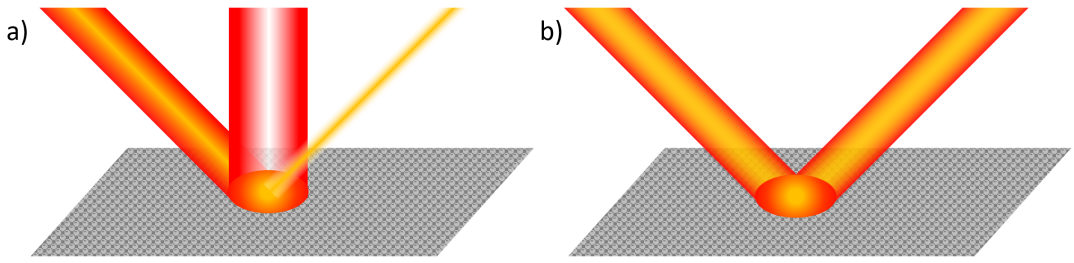

Figure 7.2: Image depicting a nonlinear, sub-diffraction limited signal. In part a), the signal arising from the center spot can be discriminated from the signal arising from the outside ring as a result of the different final momentums in the nonlinear process. Importantly, the difference in spectral emission is for image clarity, but is unnecessary. This is in contrast to part b), where the signals are both emitted in spatially overlapped directions, but are spectrally distinguishable.

the SpRS signal [47]. As the SpRS is emitted over an order of magnitude or two longer time frame, the FSRS signal outweighs the SpRS by a factor of 10^4 and needs no further treatment.

Although quantum efficiency can be enough, it is often challenging to find a case where the nonlinear signal dominates so strongly. An alternative is when the signals of the two processes are distinct enough to be separable from one another. In nonlinear optics, this can be done via conservation of momentum of the emitted signals. In this case, as depicted in Figure 7.2 a), the signal from the different regions is emitted in different directions, leading to a spatial discrimination between signals.

An alternative method is shown in Figure 7.2 b). In this instance, the beams are colinear in emission direction, but the signals can be separated based on their wavelength. For a STED-like FSRS experiment, the signals are can be discriminated by the momentum conservation[33], as in Figure 7.2, or by a combination of suppression and spectral filtering[73].

7.3 Conclusion

Nonlinear processes' ability to disentangle conjugate variables such as momentum and space and energy and time should be emphasized as an additional benefit to the already comprehensive abilities of nonlinear processes to unveil precise details of electronic, vibrational, and structural properties of materials. The important considerations for implementing a novel form of nonlinear Heisenberg breaking are distinguishability of signals as well as the relative efficiencies of the processes being driven. With this in mind, the intentional development of experiments in which nonlinearities are used to for Heisenberg breaking would be nearly as substantial as using them to probe fundamental structure. This discussion of a highly under-discussed capability of nonlinear optics should be publishable in a journal such as the American Journal of Physics.

Chapter 8

Appendices

8.1 Experimental Considerations

Generally, χ^n get increasingly smaller as n increases. As a result, higher intensity fields are required to see higher order nonlinear responses. Nothing prevents a continuous-wave (CW) laser from reaching these high intensities, the average power output would be immense and the chances of the sample not suffering damage are quite small. The alternative is to use a pulsed laser, where the average power is lower as most of the time no light is actually emitted, but when a pulse is emitted, the field intensity is substantially higher than in a CW laser. As a result, nonlinear optics and ultrafast optics and spectroscopy are intrinsically linked.

8.1.1 Pump probe

A relevant question to ask when working with ultrafast dynamics is how one resolves events that happen very quickly. The first historical solution was to take a camera in a dark room, set the exposure to a long time and to start some process and then emit a short flash of light. The camera would be reset, the trigger for the

flash would then be triggered to start at a time step after the first flash, the process would then be started again and a snap shot of the dynamics would be captured at a later part in its evolution. This process would then be repeated until the process finished and the resulting film would provide a movie of the dynamics.

This is the fundamental concept behind ultrafast spectroscopy. However, mechanical and electronic methods for triggering the light flash are limited to nanosecond time scales. This is problematic, as reactions in many atomic, molecular, and condensed phase materials typically happen on the order of tens of attoseconds, 10^{-18} s, to several picoseconds, 10^{-12} s. Pulsed laser systems present a solution to this and are now capable of generating laser pulses that can now reach into these ultrafast time scales.

The most basic form of ultrafast spectroscopy is referred to as a "pump-probe" experiment. In a pump probe experiment, much akin to the method with the cameras, two laser pulses are initially overlapped in space and time, but there is a controllable delay between the two pulses. The first pulse excites some dynamics, which can be anything from exciting a particular population to starting a chemical reaction, and thus is termed the pump pulse. The second pulse then interacts with the intermediate state, encoding a wealth of information regarding the transient states energy structure within its spectrum.

The exact nature of the information contained within the spectrum can vary drastically depending on the wavelength, energy, and duration of the pulses being used. In some of the most basic implementations of this, the polarization that is emitted will not necessarily be a nonlinear signal. However, a nonlinear signal can still be reached with this pump probe setup. This can be accomplished in the two pulse configuration if the signal looked for requires the presence of both fields, as in second harmonic generation, or if numerous photons within the same pulse interact within

the sample, as in two pulse Four Wave Mixing [36]. An alternative for observing a nonlinear response is to add additional pulses to the experiment. This can be beneficial because the geometry can be used to separate the nonlinear signals from one another.

8.1.2 Lab techniques

The implementation of any ultrafast spectroscopy experiment shares common features, such as light source selection and pulse alignment. These basic laboratory techniques will be discussed over the next section to provide clarity for the later portion of this thesis.

Laser systems

As briefly touched upon, numerous types of lasers exist. The ideal choice of laser to be used depends greatly on the application that it has been selected for. In general, the temporal resolution, spectral resolution, and wavelength should all be considered in choosing a laser system.

It would be ideal to have both high spectral and temporal resolution in an experiment. However, the Heisenberg Uncertainty Principle restricts this since energy and time do not commute [45]. As a result, it is often important to choose a laser system that gives the desired combination of spectral and temporal resolution. Continuous wave lasers have a very narrow spectral linewidth, such that they can usually be treated as a single wavelength of light being emitted. In actuality, all lasers have a finite linewidth, ranging from few Hz systems used for atomic clocks [76] to the few wavenumber lasers used in vibrational spectroscopy[55]. If signal

occurs very slowly or needs to have high energy resolution, then a Continuous Wave (CW) laser would be an ideal choice.

If the dynamics occur on a very fast time scale, a broad-band pulsed laser will be better suited. These systems have a large spectrum of colors in their bandwidth and must have a well defined phase relationship between the different colors. In an experiment, any excitation in the sample will be excited by all wavelengths in the energy spectrum of the pulse. As a result the emitted signal has poor spectral resolution.

The wavelength of the laser will determine what type of energy structure will be probed. As shorter wavelengths correspond to lower energies, microwave and infrared laser sources are often used to study materials vibrational and rotational properties[77]. The near infrared and and visible energies often correspond to valence shell electronic interactions, such as excited state absorption and chemical reaction dynamics [1, 8]. Pushing to the higher energies of the ultraviolet to and x-ray spectrum, core electron dynamics and high momentum interactions become resolvable[35].

Pulse anatomy

Accurate terminology for describing a laser pulse will be valuable to understanding how nonlinear processes affect and can be affected by the pulse shape. The time duration of a laser pulse is represented by its carrier envelope. This is the blue line in Figure 8.1 a). The usual mathematical form for this is a Gaussian or a Secant^2 function. The full width at the half maximum of the shape is used to determine the duration of the pulse.

A pulse is considered to be "transform limited" if all of the colors within its bandwidth have an overlapped peak at the same position. For a transform limited

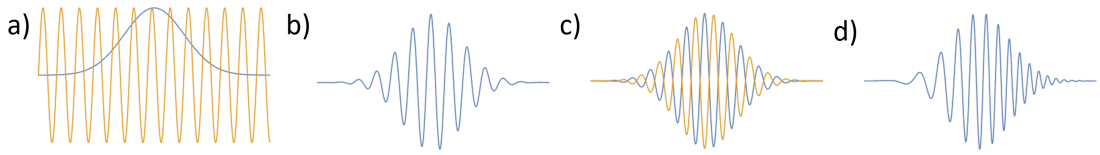

Figure 8.1: Image of the a) Gaussian envelope and the center frequency which are multiplied together to get b) a complete pulse. If the pulse is given a zeroth order dispersion, it will manifest itself as the orange line in c) where the blue line represent the original pulse. If the pulse has chirp, the center frequency will vary, as seen in d).

pulse, the entire carrier envelope should have the same frequency throughout the pulse's duration. This is the orange line in Figure 8.1 a). Multiplying the carrier envelope by an oscillation at the center frequency gives us the entire pulse, shown in Figure 8.1 b).

The exact positions of the peaks within the pulse can be altered by changing the carrier envelope phase (CEP). While this might seem like a trivial concept, it can have drastic impacts for pulses whose duration is on the order of a few center frequency cycles[34]. A shift of π in the CEP is shown in Figure 8.1 c). In this case, the superposition of the two pulses would experience complete destructive interference.

Delay stages

Numerous optical fields need to be present for any nonlinear process to occur. The temporal overlap between two ultrafast laser pulses is achieved by matching the path optical length between the two up to the scale of the shortest laser pulse duration divided by the speed of light. For a 30 fs laser pulse, this means that the paths must be aligned within about 10 μm. Translational stages and retro reflectors are the spectroscopist's tool of choice for achieving this alignment. A retro reflector reflects a beam directly back in the direction it came from with a spatial offset. The retro reflector is mounted to a movable platform, known as a delay stage, whose position

can be changed in order to match two pulses' path lengths. Ideally the stages utilize computer controlled motors with small step sizes in order to increase repeatability and accuracy of the alignment.

The improper alignment of a pulse to a delay stage can result in dynamic signal artifacts from spatial walk off of the beams on the sample. Proper stage alignment is achieved when the beam propagates parallel with the stages travel in both the transverse and vertical directions.

One can test and adjust the alignment of a translation stage by using a razor and a power meter. The razor is mounted to the delay stage and should block approximately half of the beam. A power meter should be place to measure the transmitted beam's power. The angle of the beam is then adjusted using the last mirror mount before the stage until the power meter has a constant reading over the full travel of the stage. This should be performed twice, in one instance with the razor splitting the beam laterally while adjusting the mirror's pitch, and with the razor splitting the beam vertically while adjusting the yaw. Although ideally the change in power over the stage's travel should be zero, this can be quite difficult to achieve with power fluctuations in the beams. Alignment to within 1% power change from one end to the other is a reasonable standard.

A real practical challenge to this process arises if the stage has any bow or curvature in its travel as result of manufacturing. This cannot be fixed with beam alignment and occurs in almost all stages to some extent. Accordingly, I always check that the power is the same at the beginning and end of the stage's travel. However, if the change during the stage's travel is extreme, the delay stage should be replaced.

Improper alignment of the retro reflector can lead to similar signal artifacts and must be treated with similar scrutiny. Commercial retro reflectors can be purchased

and have alignment to less than 10 arcseconds. However, the more economical option is to just make one by aligning a pair of mirrors.

To create retro reflectors, take two mirrors and adjust their pitch and yaw such that an incoming beam will be reflected roughly in the same plane as incident beams. Next, bolt one mirror to the delay so that the beam reflected from the mirror propagates roughly perpendicular to the stage's motion. Place the second mirror such that the back reflected beam is aligned roughly parallel to the incident beam. A coarse alignment can be performed by sending the beam to an iris and then adjusting the position until it remains roughly focused on the same spot on the iris. For a fine alignment, set a razor so that it blocks half of the beam's profile and place a power meter in the way of the transmitted beam. Scan the stage through its travel and adjust the second mirrors tilt and yaw until the power remains unchanged at the start and end of the travel. As before, this should be done twice where in once case the razor splits the beam laterally with the mirror's pitch is adjusted and again while the razor splits the beam vertically and the yaw is adjusted.

Pulse alignment

Once the delay stages have been properly aligned, it becomes necessary to align the pulses temporally. This is a typical challenge of ultrafast spectroscopy as the time scales encountered range between a few femtoseconds and a few picoseconds, and thus the path lengths must be aligned spatially on the scale of a few micrometers.

The general methodology for performing cross correlations revolves around the idea of looking for a signal that can only be emitted when both pulses are spatially and temporally overlapped. Often, this just means looking for a relatively easy to generate a nonlinear optical signal. By controlling the distance between the two pulses with a translational stage and searching for the nonlinear signal, one can find

the time that both pulses are spatially and temporally overlapped. This serves as the "Time zero" between the pulses. In a traditional pump probe experiment, by moving the translation stage away from time zero, one can effectively probe dynamics of the system. If a time zero is calculated incorrectly, the measured dynamic responses will not be a realistic representation of the process.

If both pulse are of identical, it is quite common to use second harmonic generation (SHG), as described in Section2.2.1, where two photons are absorbed and one is emitted at twice the energy, for the correlation. This is implemented by focusing the two beams in a non-colinear geometry onto a nonlinear crystal. The crystal should be adjusted so that its angle is in between the angle where each beam individually produces the brightest a second harmonic signal. The temporal delay between the two pulse should then be changed. When both pulses are overlapped on the crystal, a second harmonic beam will be emitted straight out, in between the two input beams. This result can be extended to performing sum frequency generation, the addition of two photons energy, in the case of two different colored pulses, but the phase matching direction can be more challenging in these cases. Additionally, if the pulses are already on the blue/green end of the spectrum, the harmonic signal will be incredibly weak as a result of absorption from the medium.

An intensity autocorrelation can be used if both pulses share identical spectrum. In this case, the two pulse are aligned colinearly. When they are both overlapped in space and time, a set of fringes will appear in the beam profile as a result of the interference of the two fields. If the pulses are different colors, one cannot search for the interference fringes between the pulses when they overlap as they will beat at the frequency difference between them. For two pulses in the visible, this means that a femtosecond photodiode would be required. Since femtosecond photodiodes don't exist, this method cannot be implemented.

The temporal alignment of two pulses of different color and duration is more challenging that in the case of identical pulses. If the pulses are of different durations, the signal that is emitted from them can only use a fraction of one pulses power to contribute to the signal, as opposed to the case where the pulses can completely overlap and drive the nonlinear response for their entire duration.

Dispersion

The index of refraction is a measure of how much light bends when passing from one medium to another. In actuality, this corresponds to the light slowing down as it propogates through different materials[34]. If one passes white light through a prism, then one will notice that the colors will be dispersed, as shown in Figure 8.2. This is a manifestation of the wavelength dependence of the index of refraction.

The wavelength dependence of light traveling through a medium presents a substantial challenge for ultrafast spectroscopy. Shorter laser pulses require precise temporal alignment of a broad bandwidth of colors[34] and as the pulse propagates through the material, the different colors of the pulse propagate at different speeds. The result is a stretching of the pulse as the different colors take longer to propogate through the optic.

It is common to describe the dispersion of the system in terms of a modulation to temporal phase of the pulse by the addition of a series of higher order polynomials[34]. A zeroth order dispersion within the pulse would be a change in the carrier envelope phase. This will not effect the pulse duration or frequency distribution, but will shift the peak positions within the pulse, as shown in Figure 8.1 c). If the modulation is linear in time, the dispersion will manifest itself as an alteration of the carrier frequency of the light uniformly through the pulse envelope. A second order dispersion, or "chirp", will mathematically be described by a quadratic time

dependence. The physical result will be a carrier frequency that varies linearly throughout the pulse, as shown in Figure 8.1d). Higher n^{th} degree terms in the expansion are referred to as the n^{th} order chirp, and will be characterized as a $(n-1)^{th}$ order modulation of the center frequency of the pulse in time.

The experimental ramifications of dispersion can be substantial. As the pulse is stretched out in time by dispersion, the temporal resolution of the experiment is reduced[34]. Additionally, as the frequencies vary in time within the pulse, the sample will not see a true broadband excitation, but rather an excitation that will vary in energy. This can lead to artifacts in spectra [11].

Pulse compression

The temporal duration of a laser pulse is determined not merely by the bandwidth of the spectrum, but also by the phase relationship between the spectral components [34]. This phase relationship will be distorted if the different colors become offset in time, as will occur as the result of dispersion in a medium. If the pulse is broad enough, the best solution is only use reflective optics in the setup. However, this is not always feasible experimentally. To compensate for this, a number of methods exist for adjusting the phase relationship to compress a pulse to its transform limit.

The most common method of pulse compression is to use a pair of prisms or gratings [34]. An experimental setup for this can be seen in Figure 8.2. The beam passes through the first prism, dispersing the different colors of light as a result of the index of refraction. The amount of compensation can be selected for by altering the distance between the first prism and second, as well as by varying the insertion of the second prism into the dispersed beam. This is shown in Figure 8.2. This method can be challenging as the correct positioning of the prisms for ideal compensation will often

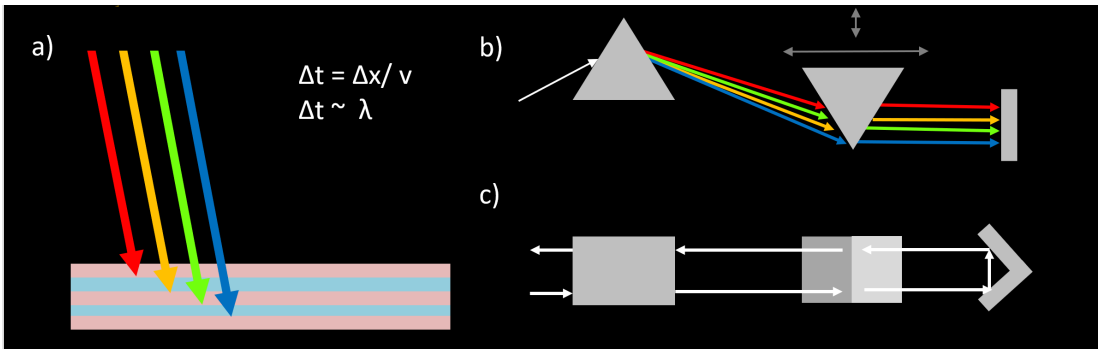

Figure 8.2: A dielectric chirped mirror a) with a linear relation between the penetration depth and the wavelength. It is easy to see that this alters the path length of the different colors in the pulse, resulting in dispersion compensation. Figure b) shows a top view of pulse compression setup for a set of prisms and c) shows it from the side. A double pass geometry, accomplished with a rooftop reflector, makes adjusting the amount of dispersion easier. Arrows represent the positioning changes needed to adjust the quantity of 2nd and 3rd order compensation.

require some trial and error or an alignment with translation stages. Additionally, the power losses of the beaming being compressed are often about 50%.

An alternative method for pulse compression is the use of chirped mirrors. By altering layers of different dielectric materials on top of one another, a wavelength dependent penetration depth can be created, as depicted in Figure 8.2. As a result, when a beam is reflected from the mirror, the different colors path lengths will be offset in time. The quantity of the compensation can be chosen by altering the number of times a pulse is reflected from the mirror. The functional form of the wavelength dependence of the penetration depth can be chosen to depend linearly on the frequency to offset dispersion, quadratically with frequency to offset the chirp, or at higher order polynomials to offset higher order chirps.

Chirped mirrors offer a few benefits over prism or grating compressors. First of all, the reflectivity of them is usually on the scale of 99%, meaning that almost no power is lost while compressing the pulse. Additionally, they are simpler to integrate

into to the beam path as the entrance angle and number of bounces are the only parameters to be adjusted. The main drawback of this technique is the cost. Often the mirrors must be custom made and can cost upwards of $10k.

Bibliography

[1] David W. McCamant, Philipp Kukura, and Richard A. Mathies. Femtosecond Broadband Stimulated Raman: A New Approach for High-Performance Vibrational Spectroscopy. *Applied Spectroscopy*, 57(11):1317–1323, 2003.

[2] Sangwoon Yoon. Watching ultrafast structural evolution : femtosecond stimulated raman spectroscopy. *Journal of Nuerological Therapy*, 3(2):70–77, 2006.

[3] Kristen E. Brown, Brad S. Veldkamp, Dick T. Co, and Michael R. Wasielewski. Vibrational dynamics of a perylene-perylenediimide donor-acceptor dyad probed with femtosecond stimulated Raman spectroscopy. *Journal of Physical Chemistry Letters*, 3(17):2362–2366, 2012.

[4] M. Yoshizawa, H. Aoki, and H. Hashimoto. Vibrational relaxation of the2Ag-excited state in all-trans-β-carotene obtained by femtosecond time-resolved Raman spectroscopy. *Physical Review B*, 63(18):180301, 2001.

[5] Shaul Mukamel and Jason D Biggs. Communication : Comment on the effective temporal and spectral resolution of impulsive stimulated Raman signals. *Journal of Chemical Physics*, 161101:1–4, 2011.

[6] Soo-y Lee, Donghui Zhang, David W Mccamant, Philipp Kukura, Richard A Mathies, Soo-y Lee, and Donghui Zhang. Theory of femtosecond stimulated Raman spectroscopy Theory of femtosecond stimulated Raman spectroscopy. *Jounral of Chemical Physics*, 3632(2004), 2016.

[7] David M Jonas. 2D spectroscopy. *Annual Review Physical Chemistry*, 2003.

[8] Steven T Cundiff. Coherent spectroscopy of semiconductors. *Optics Express*, 16(7):4639–4664, 2008.

[9] Shaul Mukamel, Yoshitaka Tanimura, and Peter Hamm. Multidimensional Coherent Spectroscopy. *Acc. Chem. Res.*, 42(9):1207–1209, 2009.

[10] Masayuki Yoshizawa and Yasuhiro Hattori. Femtoseconad time-resolved resonance Raman gain spectroscopy in polydiacetylene. *Physical Review B*, 49(18):259–262, 1994.

[11] David W Mccamant, Philipp Kukura, and Richard A Mathies. Femtosecond Stimulated Raman Study of Excited-State Evolution in Bacteriarhodopsin. *Journal of Physical Chemistry B*, 109(20):10449–10457, 2005.

[12] Xueqiong Qiu, Xiuting Li, Kai Niu, Soo-y Lee, Xueqiong Qiu, Xiuting Li, Kai Niu, and Soo-y Lee. Inverse Raman bands in ultrafast Raman loss spectroscopy. *Journal of Chemical Physics*, 164502(135), 2011.

[13] Renee R Frontiera, Anne-isabelle Henry, Natalie L Gruenke, and Richard P Van Duyne. Surface-Enhanced Femtosecond Stimulated Raman Spectroscopy. *Journal of Physical Chemistry*, pages 1199–1203, 2011.

[14] Hikaru Kuramochi, Satoshi Takeuchi, and Tahei Tahara. Ultrafast structural evolution of photoactive yellow protein chromophore revealed by ultraviolet

resonance femtosecond stimulated Raman spectroscopy. *Journal of Physical Chemistry Letters*, 3(15):2025–2029, 2012.

[15] B. G. Oscar, W. Liu, Y. Zhao, L. Tang, Y. Wang, R. E. Campbell, and C. Fang. Excited-state structural dynamics of a dual-emission calmodulin-green fluorescent protein sensor for calcium ion imaging. *Proceedings of the National Academy of Sciences*, 111(28):10191–10196, 2014.

[16] Joohyun Lee, J. Reddy Challa and David W. McCamant. Ultraviolet Light Makes dGMP Floppy: Femtosecond Stimulated Raman Spectroscopy of 2-Deoxyguanosine 5-Monophosphate. *Jounral of Physical Chemistry B*, 2017.

[17] Novoselov KS, Geim AK, Morozov SV, D Jiang, Y Zhang, Dubonos SV, Grigorieva IV, and Firsov AA. Electric Field Effect in Atomically Thin Carbon Films. *Science*, 306(5696):666–669, 2004.

[18] Kin Mak, Changgu Lee, James Hone, Jie Shan, and Tony Heinz. Atomically thin mos2: A new direct-gap semiconductor. *Physical Review Letters*, 105(13):136805, 2010.

[19] Mohammad Rahman, Kenneth Davey, and Shi-zhang Qiao. Advent of 2D Rhenium Disulfide (ReS 2): Fundamentals to Applications. *Advance Functional Materials*, 2017.

[20] K.S. Novoselov, A.K. Geim, Morozov, S.V., D. Jiang, M.I. Katsnelson, I.V. Grigorieva, S.V., Dubonos, and A.A. Firsov. Two-Dimensional Gas of Massless Dirac Fermions in Graphene. *Nature*, 438:197–200, 2005.

[21] David G Cahill, Wayne K Ford, Kenneth E Goodson, Gerald D Mahan, and Humphrey J Maris. Nanoscale thermal transport. *Applied Physics Reviews*, 93(2):793–818, 2003.

[22] Kristen Kaasbjerg, K S Bhargavi, and S S Kubakaddi. Hot-electron cooling by acoustic and optical phonons in monolayers of MoS 2 and other transition-metal dichalcogenides. *arXiv*, pages 1–15, 2014.

[23] David G Cahill, Paul V Braun, Gang Chen, David R Clarke, Shanhui Fan, Kenneth E Goodson, William P King, Gerald D Mahan, Arun Majumdar, Humphrey J Maris, Simon R Phillpot, Eric Pop, David G Cahill, Paul V Braun, Gang Chen, David R Clarke, Shanhui Fan, Kenneth E Goodson, Pawel Keblinski, William P King, Gerald D Mahan, Arun Majumdar, Humphrey J Maris, Simon R Phillpot, Eric Pop, and Li Shi. Nanoscale thermal transport ii . 2003 – 2012. *Applied Physics Reviews*, 1(011305):1–45, 2016.

[24] Gianluca Fiori, Francesco Bonaccorso, Giuseppe Iannaccone, Tomás Palacios, Daniel Neumaier, Alan Seabaugh, Sanjay K. Banerjee, and Luigi Colombo. Electronics based on two-dimensional materials. *Nature Nanotechnology*, 9(10):768–779, 2014.

[25] Yuan Cao, Valla Fatemi, Shiang Fang, Kenji Watanabe, Takashi Taniguchi, Efthimios Kaxiras, and Pablo Jarillo-Herrero. Unconventional superconductivity in magic-angle graphene superlattices. *Nature*, 556(7699):43–50, 2018.

[26] Qing Hua Wang, Kourosh Kalantar-Zadeh, Andras Kis, Jonathan N Coleman, and Michael S Strano. Electronics and optoelectronics of two-dimensional transition metal dichalcogenides. *Nature Nanotechnology*, 7(11):699–712, 2012.

[27] Rui Zhang and Rebecca Cheung. Mechanical Properties and Applications of Two- Dimensional Materials. *Intech*, 2016.

[28] Nengjie Huo, Yujue Yang, and Jingbo Li. Optoelectronics based on 2D TMDs and heterostructures. *Journal of Semiconductors*, 38(3):1–9, 2017.

[29] Xiaokun Gu and Ronggui Yang. Phonon transport in single-layer transition metal dichalcogenides : A first-principles Phonon transport in single-layer transition metal dichalcogenides : A first-principles study. *Appl. Phys. Letters*, 131903(2014), 2015.

[30] Andrea Cepellotti. *Thermal transport in low dimensions PAR*. PhD thesis, Ecole Polytechnique Federale Lausanne, 2016.

[31] Xiao-ping Luo and Hong-liang Yi. A discrete unified gas kinetic scheme for phonon Boltzmann transport equation accounting for phonon dispersion and polarization. *International Journal of Heat and Mass Transfer*, 114:970–980, 2017.

[32] Bass, editor. *Handbook of Optics IV*. McGrawHill, 2001.

[33] W Ruchira Silva, Christian T Graefe, and Renee R Frontiera. Toward Label-Free Super-Resolution Microscopy. *ACS Photonics*, 2016.

[34] Jean-Claude Diels. *Ultrashort Laser Pulse Phenomena*. Elsevier, 1996.

[35] Robert Boyd. *Nonlinear Optics*. Elsevier, 2007.

[36] Mark Siemens. *Tutorial on Multidimensional Coherent Spectroscopy*. Elsevier, 2018.

[37] Derryck T Reid, Christoph M Heyl, Robert R Thomson, Steffen Hädrich, Jan Rothhardt, and Manuel Krebs. Design criteria for ultrafast optical parametric amplifiers. *Journal of Optics*, 18(103501):33, 2016.

[38] M Bradler P Baum E Riedle. Femtosecond continuum generation in bulk laser host materials with sub-J pump pulses. *Applied Physics B*, pages 561–574, 2009.

[39] Maximilian Bradler. *Bulk continuum generation: The ultimate tool for laser applications and spectroscopy*. PhD thesis, Ludwig-Maximiliams University, 2014.

[40] Krishnan. Raman effect: History of the discover. *Journal of Raman Spectroscopy*, 1981.

[41] P O Brown, D Botstein, M Lapidot, Y Pilpel, A Mazo, J W Hodgson, S Petruk, Y Sedkov, H W Brock, J A Timmons, L Good, P Kapranov, A T Willingham, T R Gingeras, O Yazgan, J E Krebs, M E Fahey, T F Moore, D G Higgins, B Lehner, G Williams, R D Campbell, C M Sanderson, J Shendure, G M Church, H Kiyosawa, I Yamanaka, N Osato, S Kondo, Y Hayashizaki, D J Lipman, G G Carmichael, A J Simpson, S J De Souza, A A Camargo, R R Brentani, B A Williams, K Mccue, L Schaeffer, B Wold, S Edwards, D Shoemaker, and E E Schadt. Label-free biomedical imaging with stimulated raman. *Science*, 322(December):1857–1861, 2008.

[42] Dong Hoon Keum, Suyeon Cho, Jung Ho Kim, Duk-Hyun Choe, Ha-Jun Sung, Min Kan, Haeyong Kang, Jae-Yeol Hwang, Sung Wng Kim, Heejun Yang, K. J. Chang, and Young Hee Lee. Bandgap opening in few-layered monoclinic MoTe2. *Nature Physics*, 11(6):482–486, 2015.

[43] N C Dang, C A Bolme, D S Moore, and S D Mcgrane. Femtosecond Stimulated Raman Scattering Picosecond Molecular Thermometry in Condensed Phases. *Physical Review Letters*, 043001(July):1–4, 2011.

[44] David Tuschel. Raman Thermometry. *Spectroscopy*, 31(12):8–13, 2016.

[45] *Modern Quantum Mechanics*. Pearson, 2017.

[46] Jun Kojima and Quang Viet Nguyen. Single-shot rotational Raman thermometry for turbulent flames using a low-resolution bandwidth technique. *Measurement Science and Technology*, 19(1), 2008.

[47] Daniel R Dietze and Richard A Mathies. Femtosecond Stimulated Raman Spectroscopy. *Chemical Physics Review Letters*, pages 1224–1251, 2016.

[48] Toshiaki Hattori, Akira Terasaki, and Takayoshi Kobayashi. Coherent Stokes Raman scattering. *Physical Review A*, 35(2), 1987.

[49] Zhigang Sun, J. Lu, Dong H. Zhang, and Soo-Y. Lee. Quantum theory of (femtosecond) time-resolved stimulated Raman scattering. *The Journal of Chemical Physics*, 128(14):144114, 2008.

[50] Daniel R. Dreyer, Rodney S. Ruoff, and Christopher W. Bielawski. From conception to realization: An historial account of graphene and some perspectives for its future. *Angewandte Chemie - International Edition*, 49(49):9336–9344, 2010.

[51] A H Castro Neto. Charge Density Wave , Superconductivity , and Anomalous Metallic Behavior in 2D Transition Metal Dichalcogenides. *Physical Review Letters*, pages 1–4, 2001.

[52] Yanpeng Qi, Pavel G Naumov, Mazhar N Ali, Catherine R Rajamathi, Walter Schnelle, Oleg Barkalov, Michael Hanfland, Shu-Chun Wu, Chandra Shekhar, Yan Sun, Vicky Sü, Marcus Schmidt, Ulrich Schwarz, Eckhard Pippel, Peter Werner, Reinald Hillebrand, Tobias Förster, Erik Kampert, Stuart Parkin, R J Cava, Claudia Felser, Binghai Yan, and Sergey A Medvedev. ARTICLE Superconductivity in Weyl semimetal candidate MoTe 2. *Nature Communications*, 7:1–48, 2016.

[53] Bevin Huang, Genevieve Clark, Efren Navarro-moratalla, Dahlia R Klein, Ran Cheng, Wang Yao, Di Xiao, Pablo Jarillo-herrero, and Xiaodong Xu. Layer-dependent Ferromagnetism in a van der Waals Crystal down to the Monolayer Limit. *archiveX*, 2017.

[54] Michael A Mcguire, Genevieve Clark, Santosh Kc, W Michael Chance, Gerald E Jellison, Valentino R Cooper, Xiaodong Xu, and Brian C Sales. Magnetic Behavior and Spin-Lattice Coupling in Cleavable, van der Waals Layered CrCl 3 Crystals. *arXiv*, pages 1–10, 2017.

[55] Amber McCreary, Jeffrey R Simpson, Yuanxi Wang, Daniel Rhodes, Kazunori Fujisawa, Luis Balicas, Madan Dubey, Vincent H. Crespi, Mauricio Terrones, and Angela R. Hight Walker. Intricate Resonant Raman Response in Anisotropic ReS2. *Nano Letters*, page acs.nanolett.7b01463, 2017.

[56] E Ploetz, B Marx, T Klein, R Huber, and P Gilch. A 75 MHz Light Source for Femtosecond Stimulated Raman Microscopy. *Optics Express*, 17(21):18612–18620, 2009.

[57] P. Nandakumar, A. Kovalev, and A. Volkmer. Vibrational imaging Based on stimulated Raman scattering microscopy. *New Journal of Physics*, 11:0–9, 2009.

[58] Daniel C. Hannah, Kristen E. Brown, Ryan M. Young, Michael R. Wasielewski, George C. Schatz, Dick T. Co, and Richard D. Schaller. Direct measurement of lattice dynamics and optical phonon excitation in semiconductor nanocrystals using femtosecond stimulated raman spectroscopy. *Physical Review Letters*, 111(10):1–5, 2013.

[59] Weimin Liu, Longteng Tang, Breland G Oscar, Yanli Wang, Cheng Chen, and Chong Fang. Tracking Ultrafast Vibrational Cooling during Excited-State Proton Transfer Reaction with Anti-Stokes and Stokes Femtosecond Stimulated Raman Spectroscopy. *Appl. Phys. Letters*, 2017.

[60] Mateusz Plewicki and Robert Levis. Femtosecond stimulated Raman spectroscopy of methanol and acetone in a noncollinear geometry using a supercontinuum probe. *Optical Society of America*, 25(10):1714–1719, 2008.

[61] Kai Niu, Shulin Cong, Soo-y Lee, Kai Niu, Shulin Cong, and Soo-y Lee. Femtosecond stimulated Raman scattering for polyatomics with harmonic potentials : Application to rhodamine 6G. *Journal of Chemical Physics*, 054311, 2009.

[62] Philipp Kukura, David McCamant, and Richard Mathies. Femtosecond Stimulated Raman Spectroscopy. *Annual Review Physical Chemistry*, 58:461–88, 2007.

[63] G Batignani, E Pontecorvo, G Giovannetti, C Ferrante, G Fumero, and T Scopigno. Electronic resonances in broadband stimulated Raman spectroscopy. *Nature Publishing Group*, (July 2015):1–8, 2016.

[64] B Jayachander Rao, Maxim F Gelin, Wolfgang Domcke, B Jayachander Rao, Maxim F Gelin, and Wolfgang Domcke. Resonant femtosecond stimulated

Raman spectroscopy with an intense actinic pump pulse : Application to conical intersections Resonant femtosecond stimulated Raman spectroscopy with an intense actinic pump pulse : Application to conical intersections. *Jounral of Chemical Physics*, 084105, 2017.

[65] Oscar Breland G., Chen Cheng, Liu Weimin, Zhu Liangdong, and Fang Chong. Dynamic Raman Lineshapes on an Evolving Excited State Landscape : Insights from Tunable Femtosecond Stimulated Raman Spectroscopy. *Journal of Physical Chemistry A*, 2017.

[66] Lauren E Buchanan, Michael O Mcanally, Natalie L Gruenke, George C Schatz, and Richard P Van Duyne. Studying Stimulated Raman Activity in Surface-Enhanced Femtosecond Stimulated Raman Spectroscopy by Varying the Excitation Wavelength. *The Journal of Physical Chemistry Letters*, 8(2):3328–3333, 2017.

[67] Renee R. Frontiera, Sangdeok Shim, and Richard A. Mathies. Origin of negative and dispersive features in anti-Stokes and resonance femtosecond stimulated Raman spectroscopy. *Journal of Chemical Physics*, 129(6), 2008.

[68] David W Mccamant, Philipp Kukura, Sangwoon Yoon, Richard A Mathies, David W Mccamant, Philipp Kukura, Sangwoon Yoon, and Richard A Mathies. Femtosecond broadband stimulated Raman spectroscopy : Apparatus and methods. *Review of Scientific Instruments*, 4971(2004), 2004.

[69] A J Minnich. Advances in the measurement and computation of thermal phonon transport. *Journal of Physics: Condensed Matter*, page 53202, 2015.

[70] Ting Li, Zhenan Tang, Zhengxing Huang, and Jun Yu. Thermal boundary resistance between the polycrystalline graphene and the amorphous SiO2 substrate. *Chemical Physics Letters*, 2017.

[71] Zhiting Tian, Keivan Esfarjani, Junichiro Shiomi, Asegun S Henry, Gang Chen, Zhiting Tian, Keivan Esfarjani, Junichiro Shiomi, Asegun S Henry, and Gang Chen. On the importance of optical phonons to thermal conductivity in nanostructures. *Appl. Phys. Letters*, 053122(99):1–4, 2011.

[72] Stefan W Hell and Jan Wichmann. Breaking the diffraction resolution limit by stimulated emission : stimulated-emission-depletion fluorescence microscopy. *Optics Letters*, 19(11):780–782, 1994.

[73] Doyeon Kim, Dae Sik Choi, Jiwoong Kwon, Sang-Hee Shim, Hanju Rhee, and Minhaeng Cho. Selective Suppression of Stimulated Raman Scattering with Another Competing Stimulated Raman Scattering. *The Journal of Physical Chemistry Letters*, pages 6118–6123, 2017.

[74] Bruno E. Schmidt, Nicolas Thiré, Maxime Boivin, Antoine Laramée, François Poitras, Guy Lebrun, Tsuneyuki Ozaki, Heide Ibrahim, and François Légaré. Frequency domain optical parametric amplification. *Nature Communications*, 5(May):1–8, 2014.

[75] Lauren E Buchanan, Natalie L Gruenke, Michael O Mcanally, Bogdan Negru, Hannah E Mayhew, Vartkess A Apkarian, George C Schatz, and Richard P Van Duyne. Surface-Enhanced Femtosecond Stimulated Raman Spectroscopy at 1 MHz Repetition Rates. *The Journal of Physical Chemistry Letters*, 7:4629–4634, 2016.

[76] N et al Hinkley. An atomic clock with 10^{-18} precision. *Science*, 2013.

[77] E Townes. *Microwave Spectroscopy*. Dover, 1975.